CEERS

Shen, Lu; Papovich, Casey; Yang, Guang; Matharu, Jasleen; Wang, Xin; Magnelli, Benjamin; Elbaz, David; Jogee, Shardha; Alavi, Anahita; Arrabal Haro, Pablo

Published in:
Astrophysical Journal

DOI:
10.3847/1538-4357/acc944

Publication date:
2023

The Astrophysical Journal, 950:7 (21pp), 2023 June 10 https://doi.org/10.3847/1538-4357/acc944

CEERS: Spatially Resolved UV and Mid-infrared Star Formation in Galaxies at $0.2 < z < 2.5$: The Picture from the Hubble and James Webb Space Telescopes

Lu Shen[1,2], Casey Papovich[1,2], Guang Yang[3,4], Jasleen Matharu[5], Xin Wang[6,7,8], Benjamin Magnelli[9], David Elbaz[9], Shardha Jogee[10], Anahita Alavi[11], Pablo Arrabal Haro[12], Bren E. Backhaus[13], Micaela B. Bagley[10], Eric F. Bell[14], Laura Bisigello[15,16], Antonello Calabrò[17], M. C. Cooper[18], Luca Costantin[19], Emanuele Daddi[9], Mark Dickinson[12], Steven L. Finkelstein[10], Seiji Fujimoto[20,21], Mauro Giavalisco[22], Norman A. Grogin[23], Yuchen Guo[10], Benne W. Holwerda[24], Jeyhan S. Kartaltepe[25], Anton M. Koekemoer[23], Peter Kurczynski[26], Ray A. Lucas[27], Pablo G. Pérez-González[28], Nor Pirzkal[29], Laura Prichard[23], Marc Rafelski[27,30], Kaila Ronayne[1,2], Raymond C. Simons[13], Ben Sunnquist[23], Harry I. Teplitz[11], Jonathan R. Trump[13], Benjamin J. Weiner[31], Rogier A. Windhorst[32], and L. Y. Aaron Yung[33]

[1] Department of Physics and Astronomy, Texas A&M University, College Station, TX 77843-4242, USA; lushen@ustc.edu.cn
[2] George P. and Cynthia Woods Mitchell Institute for Fundamental Physics and Astronomy, Texas A&M University, College Station, TX 77843-4242, USA
[3] Kapteyn Astronomical Institute, University of Groningen, P.O. Box 800, 9700 AV Groningen, The Netherlands
[4] SRON Netherlands Institute for Space Research, Postbus 800, 9700 AV Groningen, The Netherlands
[5] Cosmic Dawn Center, Niels Bohr Institute, University of Copenhagen, Rådmandsgade 62, DK-2200 Copenhagen, Denmark
[6] School of Astronomy and Space Science, University of Chinese Academy of Sciences (UCAS), Beijing 100049, People's Republic of China
[7] National Astronomical Observatories, Chinese Academy of Sciences, Beijing 100101, People's Republic of China
[8] Institute for Frontiers in Astronomy and Astrophysics, Beijing Normal University, Beijing 102206, People's Republic of China
[9] Université Paris-Saclay, Université Paris Cité, CEA, CNRS, AIM, F-91191, Gif-sur-Yvette, France
[10] Department of Astronomy,The University of Texas at Austin, Austin, TX, USA
[11] IPAC, Mail Code 314-6, California Institute of Technology, 1200 E. California Blvd., Pasadena, CA 91125, USA
[12] NSF's National Optical-Infrared Astronomy Research Laboratory, 950 N. Cherry Ave., Tucson, AZ 85719, USA
[13] Department of Physics, 196 Auditorium Road, Unit 3046, University of Connecticut, Storrs, CT 06269, USA
[14] Department of Astronomy, University of Michigan, 1085 S. University Ave., Ann Arbor, MI 48109-1107, USA
[15] Dipartimento di Fisica e Astronomia "G.Galilei,"Universitá di Padova, Via Marzolo 8, I-35131 Padova, Italy
[16] INAF–Osservatorio Astronomico di Padova, Vicolo dell'Osservatorio 5, I-35122, Padova, Italy
[17] INAF—Osservatorio Astronomico di Roma, via di Frascati 33, I-00078 Monte Porzio Catone, Italy
[18] Department of Physics& Astronomy, University of California, Irvine, 4129 Reines Hall, Irvine, CA 92697, USA
[19] Centro de Astrobiología (CSIC-INTA), Ctra de Ajalvir km 4, Torrejón de Ardoz, E-28850, Madrid, Spain
[20] Cosmic Dawn Center (DAWN), Jagtvej 128, DK-2200 Copenhagen N, Denmark
[21] Niels Bohr Institute, University of Copenhagen, Lyngbyvej 2, DK-2100 Copenhagen Ø, Denmark
[22] University of Massachusetts Amherst, 710 North Pleasant Street, Amherst, MA 01003-9305, USA
[23] Space Telescope Science Institute, 3700 San Martin Dr., Baltimore, MD 21218, USA
[24] Physics & Astronomy Department, University of Louisville, Louisville, KY 40292, USA
[25] Laboratory for Multiwavelength Astrophysics, School of Physics and Astronomy, Rochester Institute of Technology, 84 Lomb Memorial Drive, Rochester, NY 14623, USA
[26] Goddard Space Flight Center, 8800 Greenbelt Rd., Greenbelt, MD 20771, USA
[27] Space Telescope Science Institute, 3700 San Martin Drive, Baltimore, MD 21218, USA
[28] Centro de Astrobiología (CAB), CSIC-INTA, Ctra. de Ajalvir km 4, Torrejón de Ardoz, E-28850, Madrid, Spain
[29] ESA/AURA, STScI, 3700 San Martin Drive, MD21218, USA
[30] Department of Physics and Astronomy, Johns Hopkins University, Baltimore, MD 21218, USA
[31] MMT/Steward Observatory, University of Arizona, 933 N. Cherry Ave., Tucson, AZ 85721, USA
[32] School of Earth and Space Exploration, Arizona State University, Tempe, AZ 85287-1404, USA
[33] Astrophysics Science Division, NASA Goddard Space Flight Center, 8800 Greenbelt Rd., Greenbelt, MD 20771, USA
Received 2023 January 13; revised 2023 March 8; accepted 2023 March 24; published 2023 June 6

Abstract

We present the mid-infrared (MIR) morphologies for 64 star-forming galaxies (SFGs) at $0.2 < z < 2.5$ with stellar mass $M_* > 10^9\,M_\odot$ using James Webb Space Telescope (JWST) Mid-Infrared Instrument (MIRI) observations from the Cosmic Evolution Early Release Science survey. The MIRI bands span the MIR (7.7–21 μm), enabling us to measure the effective radii ($R_{\rm eff}$) and Sérsic indexes of these SFGs at rest-frame 6.2 and 7.7 μm, which contains strong emission from Polycyclic aromatic hydrocarbon (PAH) features, a well-established tracer of star formation in galaxies. We define a "PAH band" as the MIRI bandpass that contains these features at the redshift of the galaxy. We then compare the galaxy morphologies in the PAH bands to those in the rest-frame near-ultraviolet (NUV) using Hubble Space Telescope (HST) Advanced Camera for Surveys (ACS)/F435W or ACS/F606W and optical/near-IR using HST WFC3/F160W imaging from UVCANDELS and CANDELS. The $R_{\rm eff}$ of galaxies in the PAH band are slightly smaller ($\sim$10%) than those in F160W for galaxies with $M_* \gtrsim 10^{9.5}\,M_\odot$ at $z \leqslant 1.2$, but the PAH band and F160W have similar fractions of light within 1 kpc. In contrast, the $R_{\rm eff}$ of galaxies in the NUV band are larger, with lower fractions of light within 1 kpc compared to F160W for galaxies at $z \leqslant 1.2$. Using the MIRI data to estimate the $\rm SFR_{IR}$ surface density, we find that the correlation between the $\rm SFR_{IR}$ surface density

and stellar mass has a steeper slope than that of the SFR_{UV} surface density and stellar mass, suggesting more massive galaxies having increasing amounts of obscured fraction of star formation in their inner regions. This paper demonstrates how the high-angular resolution data from JWST/MIRI can reveal new information about the morphology of obscured star formation.

Unified Astronomy Thesaurus concepts: High-redshift galaxies (734); Star formation (1569); Galaxy stellar content (621); Galaxy evolution (594)

Supporting material: figure set

1. Introduction

Star formation and quenching mechanisms are the key to understanding the cosmic star formation history (e.g., Madau & Dickinson 2014). However, it depends on a complex interplay of physical processes, including the rate at which gas accretes, cools, collapses, and turns into stars, the effect of heavy elements and dust on cooling, and stellar and active galactic nucleus (AGN) feedback mechanisms. Studies on the galaxy structure up to $z \sim 2.5$ have converged to a coherent picture that the morphology of star-forming galaxies (SFGs) are disk-dominated systems (with Sérsic 1963 indexes $n \simeq 1$–2), while quiescent galaxies are bulge-dominated (with $n \gtrsim 2$; e.g., Shen et al. 2003; Weinzirl et al. 2011; Wuyts et al. 2011).[34] By measuring the galaxy size–mass distribution, it has been found that SFGs are on average larger than quiescent galaxies at all redshifts. Meanwhile, the slope of the size–mass relation for SFGs follows $R_{\rm eff} \propto M_*^{0.22}$, which is shallower than that for late-type galaxies ($R_{\rm eff} \propto M_*^{0.75}$; e.g., van der Wel et al. 2014; van Dokkum et al. 2015). These studies quantify the relation between structure and star formation in galaxies from $z \sim 0$ up to $z \sim 3$. However, it remains unclear how the structural or size evolution proceeds.

Tracking spatially resolved star formation in galaxies will provide insight into this structural/size evolution; thus, they are linked to the dominant stellar buildup of galaxies and quenching mechanisms. Indeed, studies found that ongoing star formation traced by Hα emission occurs in disks that are more extended than those occupied by existing stars in SFGs in the redshift range of $z \sim 0.5$–2.7 (Nelson et al. 2012, 2016a; Tacchella et al. 2015; Wilman et al. 2020; Matharu et al. 2022), while the extent of star formation and stellar disks are found to be the same in the local universe (James et al. 2009; Fossati et al. 2013). However, dust obscuration posts an immense challenge in uncovering star formation activities via spatially resolved galaxy studies. As dust obscuration is more acute at shorter wavelengths, it preferentially impacts the UV and visible light emitted from stars. Therefore, the possible presence of dust content could affect the interpretation of the observed light profile in UV/optical/NIR and nebular emission, in particular for massive SFGs at $M_* \gtrsim 10^{10}\,M_\odot$, which are known to have more dust attenuation (Whitaker et al. 2012; Nelson et al. 2016b; Tacchella et al. 2018).

Most of the aforementioned studies are limited by insufficient data to measure the spatially resolved dust profiles. Some studies have measured this using Balmer-line ratios (e.g., Hα/Hβ) and rely on "stacking" to get a sufficient signal-to-noise ratio (S/N). For example, Nelson et al. (2016b) stacked the spatially resolved dust attenuation maps using the Balmer decrements (Hα and Hβ emission) from the 3D Hubble Space Telescope (HST) survey for galaxies with $M_* > 10^9 M_\odot$ and at $z \sim 1$. They found that galaxies with $M_* \gtrsim 10^{10} M_\odot$ have $A_{\rm H\alpha} \sim 2$ mag of dust attenuation obscuring the star formation in their centers, while there is less dust attenuation obscuring the emission for lower-mass galaxies with $M_* \lesssim 10^{10} M_\odot$ at all radii. In general, the Hα emission should be more attenuated than the stellar continuum, due to the addition attenuation on Hα emission depending on the dust geometry (see review Calzetti 2001). Therefore, without observations on the spatially resolved dust, the total star formation rate (SFR) and the spatial distribution of SFR and stellar remain unclear.

Other studies have used size measurements of the dust emission in the far-IR (FIR) continuum measurements, e.g., 870 μm (rest-frame $\sim$250 μm at $z \sim 2.5$) obtained from Atacama Large Millimeter/submillimeter Array (ALMA). These have generally found that the effective radii of galaxies in the rest-frame FIR are in general smaller than those of rest-frame optical or UV and revealed a more compact starburst region in these massive and/or dusty SFGs (Hodge et al. 2015; Simpson et al. 2015; Chen et al. 2017; Tadaki et al. 2017a, 2017b, 2020; Calistro Rivera et al. 2018; Gullberg et al. 2019; Hodge et al. 2019; Lang et al. 2019; Cheng et al. 2020; Gómez-Guijarro et al. 2022). However, these studies focused on the bright submillimeter galaxies and/or massive galaxies with $M_* \gtrsim 10^{11}\,M_\odot$ at high redshift $z > 1$. The spatially resolved, or at least the extent of, obscured star formation of more common galaxies with $M_* < 10^{10}\,M_\odot$ galaxies remain unknown.

The Mid-Infrared Instrument (MIRI) on the James Webb Space Telescope (JWST; Gardner et al. 2006) provide observations in the mid-infrared (MIR) region of the electromagnetic spectrum spanning the wavelength range of 7.7–21 μm. In particular, the MIRI data cover the Polycyclic Aromatic Hydrocarbons (PAHs) features at 7.7 μm up to $z \sim 1.7$ and 6.2 μm up to $z \sim 2.5$, both of them tracing photodissociation regions (PDRs) associated with H II regions (e.g., Calzetti et al. 2007). In addition, the high spatial resolution of MIRI (FWHM $= 0\farcs3$ at 10 μm, corresponding to 2.4 kpc at $z \sim 1$) enables studies of resolved morphological structures in distant galaxies for the first time.

In this paper, we use the MIRI data taken as part of the Cosmic Evolution Early Release Science (CEERS; S. Finkelstein et al. 2023, in preparation; G. Yang et al. 2023, in preparation) survey to measure the morphology of galaxies in rest-frame MIR to trace the obscured star formation region for galaxies down to stellar mass of $M_* \sim 10^9 M_\odot$ in the redshift range of $0.2 < z < 2.5$. We compare these data to data from the HST covering the rest-frame NUV for these galaxies from the UltraViolet imaging of the Cosmic Assembly Near-infrared Deep Extragalactic Legacy Survey Fields (UVCANDELS) survey, which traces their unobscured star formation. Here we focus on a comparison of the NUV and MIR morphologies as this allows us to make a more complete picture of the morphology of star formation. Meanwhile, we anchor these results against the HST Wide Field Camera 3 (WFC3) F160W

[34] Throughout we will use Sérsic (1963) indexes to model galaxy surface brightness profiles. These are defined by $I(R) = I_e \exp\{-b_n[(R/R_{\rm eff})^{1/n} - 1]\}$, where $R_{\rm eff}$ is the effective radius, n is the Sérsic index, and b_n is a constant chosen to ensure that the R_e encloses 50% of the total light.

imaging from the Cosmic Assembly Near-infrared Deep Extragalactic Legacy Survey Fields (CANDELS) covering the rest-frame optical/NIR for these galaxies, which traces the existing stars. B. Magnelli et al. (2023, in preparation) will perform a more detailed analysis of the morphologies of thermal dust using the full CEERS MIRI data (4 pointings) and focus on more massive galaxies ($M_* \gtrsim 10^{10} M_\odot$). They will also compare these to other results of the dust sizes derived from far-IR imaging from ALMA available in other fields.

This paper is laid out as follows. Section 2 provides an overview of mid-IR, optical/NIR, and UV data, and multi-wavelength catalogs. We describe the bandpasses selection, sample selection, morphology measurements, spectral energy distribution (SED) fitting and surface density of stellar mass and SFR in Section 3. In Section 4, we present our results. We discuss the robustness of our results and physical implications in Section 5. We conclude with a summary in Section 6. Throughout this paper, all magnitudes, including those in the IR, are presented in the AB system (Oke & Gunn 1983; Fukugita et al. 1996). We adopt a standard concordance Lambda cold dark matter (ΛCDM) cosmology with $H_0 = 70$ km s^{-1}, $\Omega_\Lambda = 0.70$, and $\Omega_M = 0.30$.

2. Survey and Data

2.1. CEERS

CEERS (S. Finkelstein et al. 2023, in preparation) is an Early Release Science (ERS) program (Proposal ID #1345) that will cover a total ~100 sq. arcmin of the Extended Groth Strip (EGS; Davis et al. 2007) field. This field is one of the five legacy fields of CANDELS (Grogin et al. 2011; Koekemoer et al. 2011) and partially covered by the 3D HST Treasury Survey (Skelton et al. 2014; Momcheva et al. 2016). CEERS will obtain observations in several different modes with the JWST, including NIRCam imaging (Bagley et al. 2022), MIRI imaging (G. Yang et al. 2023, in preparation), and NIRSpec multiobject spectroscopic observations (see P. A. Haro et al. 2023, in preparation).

The MIRI imaging of CEERS includes seven filters (F560W, F770W, F1000W, F1280W, F1500W, F1800W, and F2100W). The first set of CEERS observations were taken on 2022 June 21 in four pointings, named CEERS1, CEERS2, CEERS3, and CEERS6 (see Table 1 in Bagley et al. 2022). These included MIRI imaging with NIRCam in parallel. In this paper, we focus on the MIRI imaging in CEERS1 and CEERS2, which received coverage in the filters covering longer wavelengths (F770W, F1000W, F1280W, F1500W, F1800W, and F2100W), covering important rest-frame mid-infrared emission features for galaxies at high redshift (CEERS3 and 6 pointings cover the shorter-wavelength MIRI filters, F560W and F770W; see Papovich et al. 2022). In particular, the MIRI observations covered the PAH feature at 7.7 μm for galaxies up to $z = 2$).

2.2. Mid-IR Imaging and Catalog

A description of the properties of the MIRI data and the reduction of these data will appear elsewhere (G. Yang et al. 2023, in preparation). We summarize the steps here. The data were processed using JWST `calibration pipeline` (v1.7.2) using mostly the default parameters for stage 1 and 2. We then modeled the background by taking the median of all the other images taken in the same bandpass but at different fields and/or dither positions. We then subtracted this background from each image. The astrometry is corrected by matching to the CANDELS HST imaging (Koekemoer et al. 2011; Bagley et al. 2022 [35]) prior to processing the images at stage 3 of the pipeline. This produced the final science images, weight maps, and uncertainty images (the latter include an estimate for correlated pixel noise; see G. Yang et al. 2023, in preparation) with a pixel scale of 0.″09, registered to the HST/CANDELS v1.9 WFC3 images.

The MIRI photometry is measured for sources detected in the original CANDELS HST/WFC3 catalog from Stefanon et al. (2017). This is appropriate as our primary interest here is in studying the MIRI morphologies and comparing them to the HST rest-frame NUV and optical data. To measure fluxes, we use `TPHOT` (Merlin et al. 2016), which uses an image with higher angular resolution (in this case the HST/WFC3 F160W detection image, which has a point-spread function (PSF) with FWHM of ≃0.″2) as a prior for photometry in images with lower angular resolution (in this case the MIRI images, which have a PSF with FWHM of ≃0.″2–0.″5). The PSF for each MIRI band is constructed using WebbPSF. We then constructed kernels to match the PSF of the F160W data to the MIRI bands. With these, we performed source photometry with `TPHOT`. This provides MIRI flux densities and uncertainties for each source in the CANDELS HST/F160W catalog, which we use as our MIRI catalog.

2.3. UV Imaging and Catalog

We adopted the HST WFC3/F275W and Advanced Camera for Surveys (ACS)/F435W imaging as part of UVCANDELS Hubble Treasury program (GO-15647, PI: H. Teplitz), which covers four of the five premier CANDELS fields (GOODS-N, GOODS-S, COSMOS, and EGS). The primary WFC3/F275W imaging reached $m \leqslant 27$ AB mag for compact galaxies (SFR $\sim 0.2\ M_\odot\ \mathrm{yr}^{-1}$ at $z = 1$), and the coordinated parallel ACS/F435W imaging reached $m \leqslant 28$ AB mag. We adopt two methodologies to measure the F275W and F435W fluxes, consistent with the previous measurements at other wavelengths (X. Wang et al. 2023, in preparation). First, we adopt the conventional hot+cold method based on object near-infrared isophotes and PSF matching following the CANDELS methodology, as in Stefanon et al. (2017). We also derive the UV-optimized aperture photometry method based on object optical isophotes aperture, following the work done in the Hubble Ultra-Deep Field UV analysis (Teplitz et al. 2013; Rafelski et al. 2015). By using smaller optical apertures without degradation of the image quality, our UV-optimized aperture photometry method reaches the expected 5σ point-source depth of 27 AB mag in F275W, deeper by ~1 AB mag than the depth reached by the conventional hot+cold method. On average, our UV-optimized photometry yields a factor of 1.5× increase in S/N in the F275W band, with higher increase in brighter extended objects. Henceforth, we take the F275W and F435W photometry obtained from the latter method as our default measurements, which complement the preexisting CANDELS photometric catalog presented in Stefanon et al. (2017).

2.4. Optical/Near-IR Imaging and Catalog

For the analysis in this paper, we adopt the multiwavelength photometric catalog from HST observations from Stefanon et al.

[35] https://ceers.github.io/releases.html

(2017; "S17 catalog" hereafter) as our primary catalog for our study here. This catalog provide measurements of the photometric redshifts and stellar population parameters of galaxies in the EGS field, using broad/median-band UV/NIR data spanning from 0.4 to 8 μm, taken by six different instruments, including Canada–France–Hawaii Telescope (CFHT)/MegaCam, NOAO Extremely Wide Field Infrared Imager (NEWFIRM)/NEWFIRM, CFHT Wide-field InfraRed CAMera (WIRCAM), HST/ACS, HST/WFC3, and Spitzer Infrared Array Camera (IRAC). The multiband photometric data were independently analyzed by 10 different groups, each one using a different set of code and/or SED templates, including FAST (Kriek et al. 2009), HyperZ (Bolzonella et al. 2000), Le Phare (Ilbert et al. 2006), WikZ (Wiklind et al. 2008), SpeedyMC (Acquaviva et al. 2012), and other available codes (Fontana et al. 2000; Lee et al. 2010). The final photometric redshifts are the median of these 10 photometric redshifts. The final stellar masses are computed as the median of the results from the six sets, which adopted an exponentially declining star formation history (SFH) and the Chabrier (2003) initial mass function (IMF), without considering nebular emission contamination (M2, M6, M10, M11, M13, and M14 in Table 4 of Stefanon et al. 2017). Note that the photometric redshifts and stellar mass do not incorporate the MIRI data. However, we do not observe significant differences between the stellar mass from S17 and the stellar mass from the Code Investigating GALaxy Emission (CIGALE) SED fitting which includes MIR and FUV data (see Section 3.4). Therefore, for this analysis, we adopt the final photometric redshifts and stellar masses presented in the "zbest" and "M_med" columns in the S17 catalog and their associated uncertainties.

We then remove AGN using the "AGNflag" in S17, which flags AGN by crossmatching to sources in the Chandra X-ray data from the All-Wavelength Extended Groth Strip International Survey (AEGIS) project (AEGIS-X Wide, Nandra et al. 2005; Laird et al. 2009; and AEGIS-XD, Nandra et al. 2015). We also consider galaxies with AGN that are missed by the X-ray data. We search for these using the CIGALE SED fitting, and remove six additional galaxies where CIGALE finds that an AGN component could contribute more than 10% to the total IR luminosity (see Sections 3.2 and 3.4).

2.5. Additional Mid-IR/Far-IR Imaging and Catalog

In addition, we adopt the IRAC 3.6+4.5 μm selected multiwavelength catalog that contains Spitzer Multiband Imaging Photometer for Spitzer (MIPS) 24 μm and 70 μm fluxes from Barro et al. (2011; "B11 catalog" hereafter). These MIPS data are obtained as part of the Guaranteed Time Observations (GTO, PI: Fazio) and the Far-Infrared Deep Extragalactic Legacy Survey (FIDEL). The 5σ limiting magnitude of MIPS 24 μm and 70 μm are 60 μJy and 3.5 mJy, respectively. We then crossmatch the S17 catalog to the B11 catalog using a 1″ radius.

3. Sample Selection and Methods

3.1. Bandpass Selection

We take advantage of the fact that the JWST/MIRI, HST/F160W, F606W, and F435W imaging are dominated by emission that originates from different regions in distant galaxies (i.e., massive stars and long-lived stars). Here, we select bands specifically to best isolate them. PAH emission arises from PDR around H II regions of young, massive stars. Thus, PAH emission traces star formation. Because the PAHs emit at the mid-IR wavelengths, they are much less affected by dust attenuation and therefore probe more obscured star formation. Previous work has shown that the integrated PAH luminosity–SFR relation has been calibrated for galaxies up to $z \sim 0.4$ (Shipley et al. 2016; Xie & Ho 2019). The total PAH emission can contribute 10%–20% of the total IR luminosity, and the 7.7 μm PAH feature, the strongest PAH feature, may contribute ~50% of the total PAH emission (e.g., Smith et al. 2007; Wu et al. 2010; Shipley et al. 2013). The next relative strong PAH feature is at 6.2 μm, which has the benefits of being relatively isolated with little contamination from nearby features and observable in galaxies at higher redshift up to $z \sim 2.5$ with MIRI. In our study, we select one or two MIRI bandpasses that contain the rest-frame 6.2 and/or 7.7 μm PAH features for each galaxy, as shown in Figure 1. We refer to them as the "PAH bands." We measure the morphology of galaxies in these PAH bands and interpret them as the morphology of obscured star formation regions.

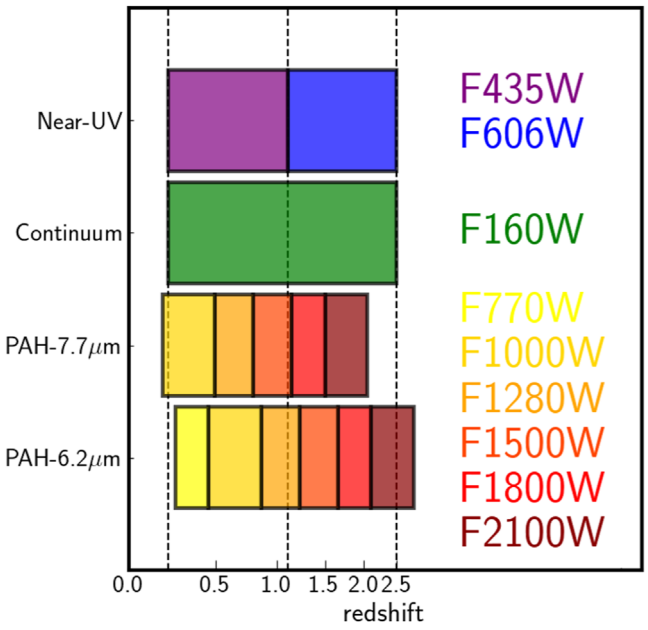

Figure 1. Selection of JWST/MIRI and HST bandpasses as PAH, NUV bands, and F160W for morphological measurements of galaxies at $0.2 < z < 2.5$. For each galaxy, we select the PAH band(s) from one or two MIRI bands that contain the rest-frame 7.7 and 6.2 μm PAH features. The yellow to red color shaded regions represent the redshift coverage of MIRI bandpasses. We adopt the HST/F160W for all galaxies, as it covers their rest-frame optical/NIR regime, corresponding to stellar continuum. We use either the HST/WFC3 F435W bandpass (for galaxies at $z < 1.1$ (purple shaded)) or the HST/ACS F606W bandpass ($z > 1.1$ (blue shaded)) as the NUV band that contain the rest-frame NUV of these galaxies, which traces the unobscured star formation. Three relevant redshifts ($z = 0.2$, 1.1, 2.5) in the band selection are marked as vertical dashed lines.

To trace the profile of unobscured star formation, we use either HST/F435W or HST/F606W for galaxies at $z \leqslant 1.1$ or $z > 1.1$, respectively, which covers the rest-frame near-UV (NUV) regime of galaxies (named the "NUV band"). Note that, ideally, the rest-frame far-UV should be used, which tie more closely to massive stars. However, due to the shallower depth of the F275W imaging and the complex far-UV structure, most of galaxies have lower S/N, and/or are resolved into a few star-forming clumps (Mehta et al. 2022). Thus, we choose to measure the NUV morphology. For the profile of stellar continuum, we adopted the HST WFC3/

F160W from CANDELS, which covers the rest-frame optical regime of galaxies at $z \sim 1$. The bandpass selection of the PAH band, NUV band, and F160W are summarized in Figure 1. Figure 2 displays the HST and JWST data and false color images for selected galaxies. The complete figure set of the false color images for galaxies in the final sample (64 images) is available in the online journal.

3.2. Sample Selection

To construct our sample, we start with the MIRI fluxes for sources in the S17 catalog. We incorporated spectroscopic redshifts ($z_{\rm spec}$) from various spectroscopic surveys, including the DEEP2 Galaxy Redshift Survey (Newman et al. 2013), the DEEP3 Galaxy Redshift Survey (Cooper et al. 2012; Zhou et al. 2019), the Multi-Object Spectrometer For Infra-Red Exploration Deep Evolution Field (MOSDEF) survey (Kriek et al. 2015), and the Complete Calibration of the Color-Redshift Relation (C3R2) survey (Masters et al. 2017). We selected sources with F160W magnitude <26.6 AB magnitude (this is the 90% completeness for point sources), photometric redshift $z_{\rm phot} \leqslant 2.5$ ($z_{\rm spec}$ when available), and without any AGN flags (Stefanon et al. 2017). The redshift cut is based on the redshift coverage of MIRI bandpasses for 6.2 μm PAH band (see Figure 1). We then selected galaxies with detection $>5\sigma$ in their selected MIRI bands (see Section 3.1). To select SFGs, we adopted the *UVJ* color–color separation as a function of the redshift from Williams et al. (2009; see Figure 3). These give us a sample of a total of 161 MIRI-detected SFGs.

For our study we need to derive measurements on the morphological parameters in multiple bandpasses, the NUV band, F160W, and PAH band(s). This requires sufficient S/N in each bandpass. We therefore model the morphological parameters in all bands for the sample of 161 MIRI-detected SFGs using GALFIT (see more details in Section 3.3), and we refine our sample to include only objects for which the GALFIT model fit converges in the NUV band, PAH band, and F160W.

We first model the morphologies of 161 MIRI-detected SFGs in the PAH bands (the one or two MIRI imaging that contain the rest-frame 6.2 and 7.7 μm PAH features) using GALFIT, as discussed in Section 3.3. We obtain 106 with successful morphological measurements in the PAH band(s). The remaining sources where GALFIT fails to converge have in general lower S/Ns. This limits our sample of SFGs in S/N to $\gtrsim$12–13 (see Figure 4). For galaxies that have successful morphological measurements in both of the MIRI bands (i.e., the two that contain the 6.2 and 7.7 μm PAH emission), we adopt the fits from the band with higher S/N in flux density. For the majority of our galaxies (76 out of 106 MIRI-detected SFGs), we adopt the morphological measurements using the PAH band that contains the rest-frame 7.7 μm PAH feature. This is primarily because the 7.7 μm PAH feature dominates the total PAH emission (e.g., Smith et al. 2007). We note that choosing to adopt PAH morphologies measurements at either rest frame 6.2 or 7.7 μm does not affect any result shown in this paper.

We then model the morphologies of these 106 MIRI-detected SFGs in the NUV band (either the HST WFC3/F435W or ACS/F606W) and F160W images using GALFIT (see Section 3.3). Of these, 83 SFGs have successful GALFIT model fits measured in all three bands (the NUV band, PAH band, and F160W). There are 14 galaxies that have morphologies where GALFIT is successful in only F160W and the PAH band, but fails in the NUV band (again, because the S/N is too low in the latter). Of these galaxies where GALFIT is unsuccessful in the NUV band, they are located in the dusty region of the *UVJ* color–color diagram and are more massive with median stellar mass of $\langle M_* \rangle = 10^{10.3} M_\odot$ than galaxies having secure sizes measured in all three bands ($\langle M_* \rangle = 10^{9.7} M_\odot$; see Figure 3). This is most likely due to the higher dust attenuation in these galaxies absorbing most of NUV light. Due to the small number of these galaxies, we exclude them in the analyses of this paper. However, we defer an analysis of these galaxies to a future study (B. Magnelli et al. 2023, in preparation). There are seven additional galaxies where the GALFIT model is successful in the NUV and PAH bands, but fails in F160W, and two more galaxies where GALFIT fails in both the F160W and NUV band. Due to the small number of these galaxies and the primary focus of this paper, we also exclude them in the analyses of this paper.

We impose a stellar mass selection of $\log(M_*/M_\odot) \geqslant 9$, where the sample is highly complete (S17 reports that $\log(M_*/M_\odot) \geqslant 9$ is the 90% completeness of point-source detection at $z \sim 1$ assuming a passively evolving simple stellar population (SSP) model Bruzual & Charlot (2003) with $A_V = 3$ mag). This stellar mass selection effectively removes galaxies with low S/N in the PAH band(s) and limits the sample to object where more than ~10% of the sample has a successful GALFIT model fit (Figure 4). Matharu et al. (2022) found that size measurements in CANDELS-like HST imaging are less reliable for galaxies at these redshifts with $M_* \lesssim 10^9 M_\odot$ (this is primarily because the sizes of the galaxies are small and approaching the resolution limit of the HST WFC3 image). We therefore apply this mass limit to our study here.

Finally, we remove six AGN candidates identified as $f_{\rm AGN} \geqslant 0.1$ from the CIGALE SED fitting (see Section 3.4). Our final sample includes 64 MIRI-detected SFGs at $0.2 < z < 2.5$ with morphological measurements in the NUV band, PAH band, and F160W. This includes 14 and 48 galaxies with their PAH morphologies measured at rest-frame 6.2 μm and 7.7 μm, respectively. There are 26 out of 64 have spectroscopic redshifts. The median uncertainties on photometric redshift of our final sample is 0.12. A summary of the sample selection and number of galaxies is provided in Table 1. The median redshift and stellar mass and their 16th/84th percentiles of our final MIRI-detected SFGs are listed in Table 2. The scatter plot of stellar mass and redshift for MIRI-detected SFGs, those with secured morphologies measured in all three bands, and the final sample are shown in Figure 3.

We note a potential bias in the sample selection toward SFGs with moderate dust and against very dusty SFGs because of excluding NUV-undetected sources. Our goal is to focus on the comparison between NUV and PAH morphologies. B. Magnelli et al. (2023, in preparation) will focus on the morphology studies from the MIRI data that include objects undetected in the NUV band.

3.3. The Morphology Measurements

We use GALFIT (Peng et al. 2002, 2010) for the morphology measurements following the two-GALFIT-run approach from Matharu et al. (2019, 2022), which leads to a high level of agreement with published size measurements (see more details in Matharu et al. 2019). For each galaxy, we create $10'' \times 10''$ cutouts of the NUV band, PAH band, and F160W and associated error images, centered on its F160W coordinates. We adopt a single 2D single-component Sérsic and a background sky profiles to fit each cutout in two iterations. A

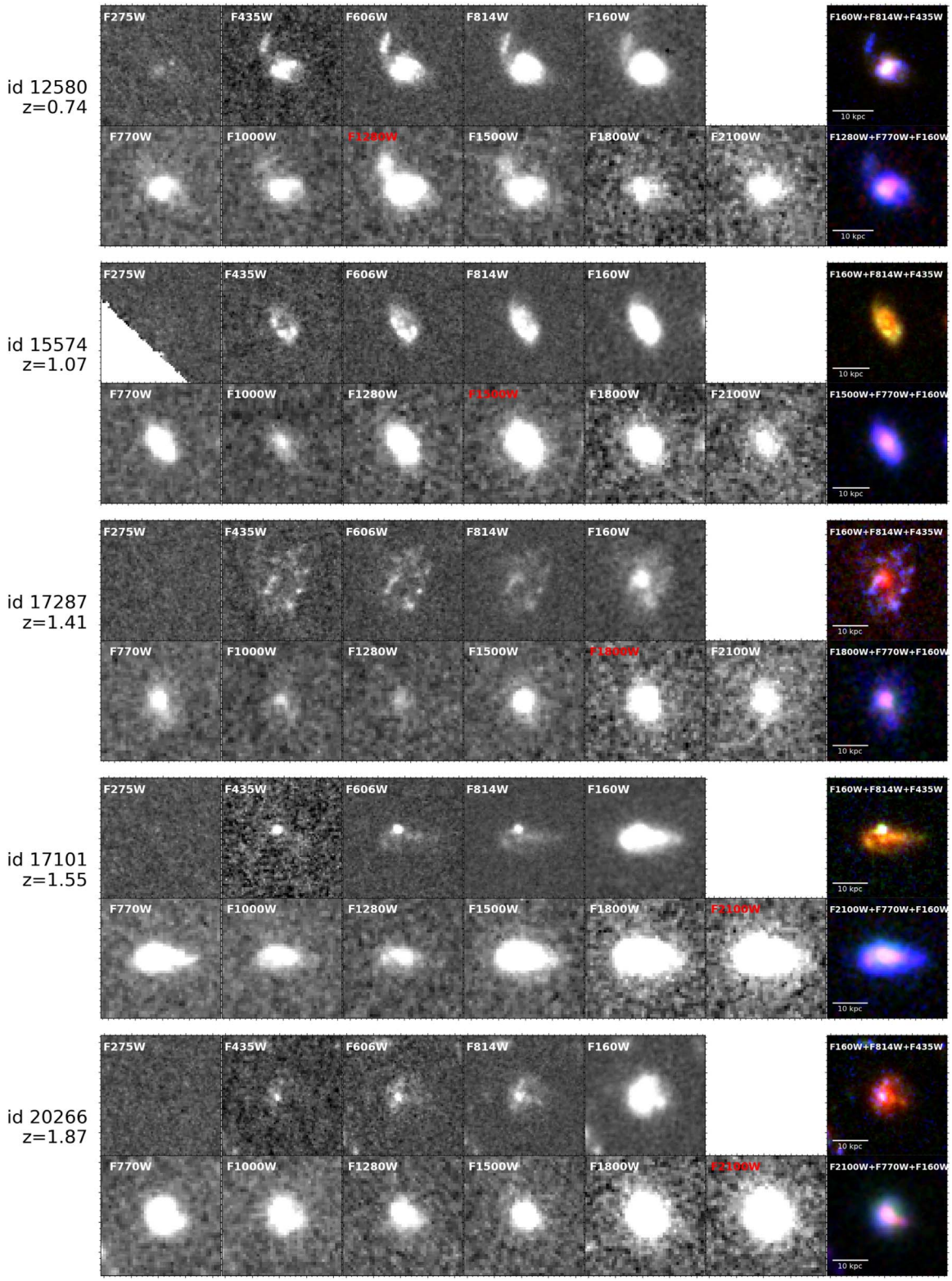

Figure 2. Example of the postage stamps ($2'' \times 2''$) centered on the selected galaxies in all available HST and JWST images, ordered by increasing redshift. In the rightmost panels, we show false color image using HST F435W+F814W+F160W (top) and F160W/HST+F770W/JWST+PAH band at rest-frame 7.7 μm from MIRI/JWST (bottom) as blue+green+red false color, respectively. For each galaxy, the PAH band at rest-frame 7.7 μm is marked by red label. The ID and photometric redshift from Stefanon et al. (2017) are marked on the left.

(The complete figure set (64 images) is available.)

PSF image is included in every GALFIT fit to account for the image resolution limit. The error images are used as sigma images when running GALFIT. In the first iteration, all parameters are kept to free. In the second iteration, we fix the shape parameters (x, y center, axis ratio, position angle) and sky level to the values from the first iteration, and we refit for the

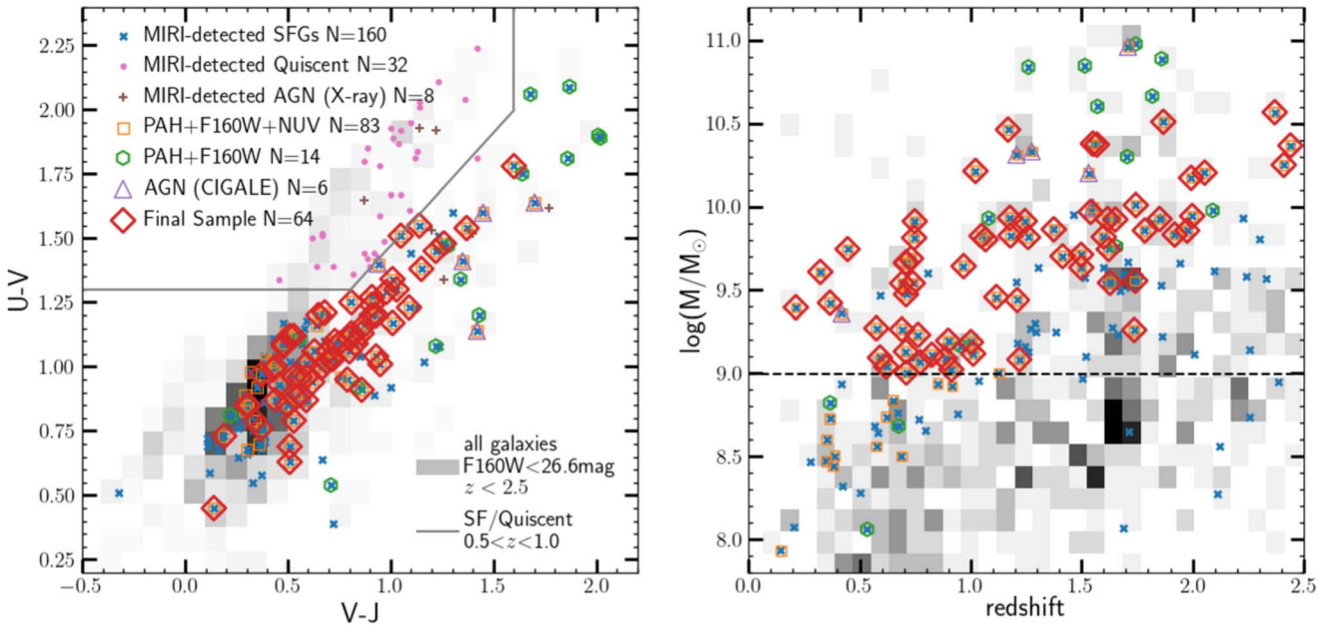

Figure 3. A *UVJ* color–color (left) and stellar mass–redshift (right) phase diagram of the final sample. In each panel, MIRI-detected SFGs (blue cross), *UVJ*-selected quiescent galaxies (pink dots), and AGN identified by X-ray detections (brown pluses) are overlaid on the 2D histogram of all photometric galaxies at $z < 2.5$. Open symbols mark those MIRI-detected SFGs with successful GALFIT fits in all three of the PAH, NUV, and F160W bands (orange), and only in PAH band and F160W (green). Additional AGN candidates identified by CIGALE are marked by purple triangles. The final sample are marked by red open diamonds. The solid gray lines in the left panel show the separation for galaxies at $0.5 < z < 1.0$ applied to our sample to select SFGs (Williams et al. 2009). The dashed back line in the right panel indicates the stellar mass selection limit.

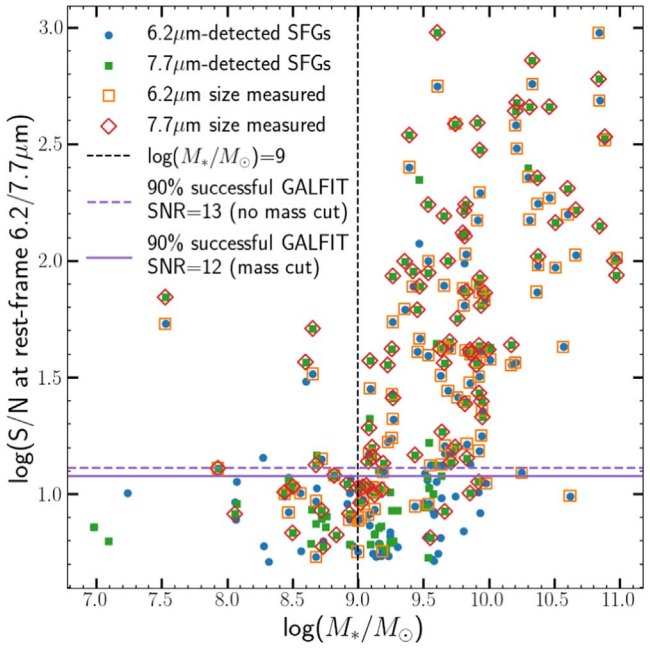

Figure 4. Signal-to-noise ratio of the JWST/MIRI detection in the PAH band (rest-frame 6.2/7.7 μm)) as a function of the stellar mass for the MIRI-detected SFGs. The blue dots and green squares correspond to MIRI-detected SFGs selected with rest-frame 6.2 μm and 7.7 μm MIRI flux $>5\sigma$, respectively. The open red and orange symbols mark SFGs with secure morphology measurements using GALFIT. The black vertical line marks the stellar mass cut at $M_* \geqslant 10^9 M_\odot$. The purple dashed and solid lines show the S/N of MIRI fluxes for which 90% of galaxies have successful GALFIT fits.

effective radius ($R_{\rm eff}$), Sérsic index (n), and magnitude. We exclude those GALFIT outputs marked with an asterisk on either side of any value.

We visually examine all the GALFIT results. There are seven galaxies that appear to be involved in mergers/interactions, including three galaxies with each having a close companion (id 17353, id 17423, id 20784) and four galaxies with evidence of tidal features (id 12363, id 12580, id 17309, and id 20237). For the three galaxies with companions, we add an additional single Sérsic profile for the adjacent galaxy in the GALFIT input and refit with the two-GALFIT-run. For the four galaxies with evidence of tidal features, their minor components are much fainter than the main structures; thus we use one Sérsic profile to model the main structure of these galaxies. Examples of GALFIT fits are shown in Figure 5. The S/N of the PAH band (rest-frame 6.2/7.7 μm) as function of the stellar mass are

Table 1
Summary of Sample Selection

Selection Criteria (1)	Num. of Gals. (2)
Sources in the parent MIRI catalog	964
m(F160W) $\leqslant$ 26.6 AB and $z_{\rm phot}(z_{\rm spec}) \leqslant 2.5$	683
AGN flag = 0	675
Rest-frame 6.2 or 7.7 μm PAH band S/N > 5	192
UVJ-selected, MIRI-detected SFGs[a]	161
Successful GALFIT model fit in MIRI PAH band(s)	106 (76/30)
Successful GALFIT model fit in PAH band(s), F160W, and NUV band	83 (65/18)
$\log(M_*/M_\odot) \geqslant 9$	70 (56/14)
Final Sample with $f_{\rm AGN} < 0.1$ from CIGALE	64 (50/14)

Notes. (1) Selection criteria and sample name; note that the selection criteria are cumulative. (2) Total number of galaxies. Numbers in the parentheses are number of galaxies use morphology measured in rest-frame 7.7 μm or 6.2 μm, respectively.
[a] We remove "quiescent" galaxies following the rest-frame color selection of Williams et al. (2009).

Table 2
Parameter Ranges Used in the SED Fitting with CIGALE

Parameter	Values
Star formation history (sfhdelayed)	
τ [Gyr]	0.1, 0.3, 1, 3, 5, 10
Age [Gyr]	0.1, 0.5, 1, 3, 5, 7, 10
Simple stellar population (Bruzual & Charlot 2003)	
IMF	Chabrier (2003)
Metallicity	0.02
Dust attenuation (Calzetti et al. 2000)	
$E(B-V)_l$	0.01, 0.05, 0.1, 0.2, 0.3, 0.5, 0.7 0.9
$E(B-V)_{\rm factor}$	0.44
Amplitude of the UV bump	0, 1.5, 3
Slope of the power law	−0.5, −0.25, 0
Dust emission (Draine et al. 2014)	
Mass fraction of PAH (%)	0.47, 2.50, 4.58, 6.63
Minimum radiation field	0.1, 1, 10, 30
Power slope $dU/dM \propto U^{-\alpha}$	2.0
Dust fraction in PDRs	0.05
AGN emission (SKIRTOR)	
Viewing angle	30, 70
$f_{\rm AGN}$	0–0.9

shown in Figure 4. 90% of galaxies have successful morphology measurements with S/Ns of 13 and 12 before and after the stellar mass cut at $M_* \geqslant 10^9 M_\odot$. Meanwhile, 72% of galaxies with $M_* \geqslant 10^9 M_\odot$ have successful GALFIT model fits in the PAH band. The number of galaxies with successful GALFIT fits in the PAH band, NUV band, and F160W are listed in Table 1.

In this paper, we mainly use the $R_{\rm eff}$ (the effective semimajor axis) and n measured from GALFIT. To account for the covariance of $R_{\rm eff}$ and n, we adopt a parameter to describe the fraction of light contained within 1 kpc following (Graham & Driver 2005; Graham et al. 2005; Ji & Giavalisco 2022; Matharu et al. 2022) calculated as

$$f_{1\ \rm kpc} = \frac{\gamma(2n,\ b_n R_{\rm eff}^{-1/n})}{\pi}, \quad (1)$$

where $\gamma(2n,\ b_n R_{\rm eff}^{-1/n})$ is the lower incomplete gamma function and b_n is a n-dependent normalization parameter that satisfies $\Gamma(2n) = \gamma(2n,\ b_n)$. We adopted approximation values of b_n as functions of n derived in analytical expressions from Ciotti & Bertin (1999) and MacArthur et al. (2003).

We employed a Monte Carlo simulation to estimate the uncertainties of these morphological properties derived from GALFIT. For each iteration we added random noise to each MIRI image using the error image for the original image. We then rerun GALFIT by fixing the shape parameters and sky level to the values obtained from the original image, and allowing the $R_{\rm eff}$, n and magnitude to vary. For galaxies without spectroscopic redshift, we also perturb the photometric redshift by drawing a new redshift from a Gaussian distribution with the mean redshift set to $z_{\rm phot}$ and σ set to one-half of the difference between the 16th and 84th percentiles of the photometric redshift. We then reselect the appropriate MIRI band that contains the PAH feature for each galaxy at the "new" redshift. We run the Monte Carlo with 100 iterations for each band of each galaxy and adopt the 16th and 84th percentiles of the mock $R_{\rm eff}$, n, and $f_{1\ \rm kpc}$ as their uncertainties on each quantity. In this way we incorporate the uncertainties of the image, using the photoemtric redshift into our analysis.

3.4. CIGALE SED Fitting

We employed the SED fitting code CIGALE (Boquien et al. 2019; Yang et al. 2020) in order to constrain possible AGN contribution to the IR luminosity of our samples and to estimate the IR and FUV luminosities in a self-consistent framework that considers the energy balance between the UV/optical and IR. In detail, we adopted a delayed exponential SFH allowing the τ and stellar age varying from 0.1–10 Gyr and 0.1–10 Gyr, respectively. We assumed a Chabrier (2003) IMF and the stellar population synthesis models presented by Bruzual & Charlot (2003) with solar ($Z_\odot$) metallicity. The dust attenuation follows Calzetti et al. (2000)'s extinction law allowing color excess $E_s(B-V)$ to vary from 0 to 0.4. The amplitude of the absorption UV bump feature produced by dust at 2175 Å and the slope of the power law are allowed to vary from 0–3 and −0.5–0, respectively. For the dust emission module, we adopted the dust templates of Draine et al. (2014). This module models the dust emission with two components, the diffused emission and the PDR emission associated with star formation. We allow the mass fraction of PAH to vary between four different values and the minimum radiation field ($U_{\rm min}$) to vary between 0.1, 1.0, 10, 30. For the AGN module, we adopt the SKIRTOR template. We retain the default parameters in the AGN module, other than setting the viewing angle i to 30° and 70° for type 1 and type 2 AGNs, respectively, and a full range of AGN fraction ($f_{\rm AGN}$) from 0 to 0.9, a fraction that denotes the contribution from the AGN to the total IR luminosity. More details of the parameter setting are shown in Table 2. We adopt the "PDF analysis" method in CIGALE to compute the likelihood (χ^2) for all the possible combinations of parameters and generate the marginalized probability distribution function for each parameter and each galaxy.

We run CIGALE on the photometry measured from the ground-based observations: u^*, g', r', i, z' from CFHT/MegaCam and Ks from CFHT/WIRCam, as well as from the space-based observations: six HST bands (F275W, F435W, F606W, F814W, F125W, F160W), three IRAC/Spitzer channels (3.6, 4.5, and 5.8 μm), six JWST MIRI bands (F770W, F1000W, F1280W, F1500W, F1800W, and F2100W) and MIPS/Spitzer at 24 μm and 70 μm. The ground-based, HST and IRAC data are adopted directly from S17. The MIPS data are included from the catalog provided by Barro et al. (2011). For galaxies without MIPS detections, we adopted the 5σ as an upper limit. Furthermore, we have excluded the IRAC/Spitzer channel at 8 μm because it is similar to the MIRI F770W, but the latter is substantially deeper. Examples of the best-fitted SEDs are shown in Figure 6. We adopt the Bayesian results of IR luminosity ($L_{\rm IR}$) and FUV luminosity ($L_{\rm FUV}$) and their associated errors from CIGALE for estimating IR/UV-based SFR and surface density of SFR (see Section 3.5).

In addition, we adopt the $f_{\rm AGN}$ from CIGALE to select galaxies that appear to host an AGN with $f_{\rm AGN} \geqslant 0.1$, and star formation dominated galaxies with $f_{\rm AGN} < 0.1$ following Shen et al. (2020). CIGALE calculates $f_{\rm AGN}$ as the fraction of the

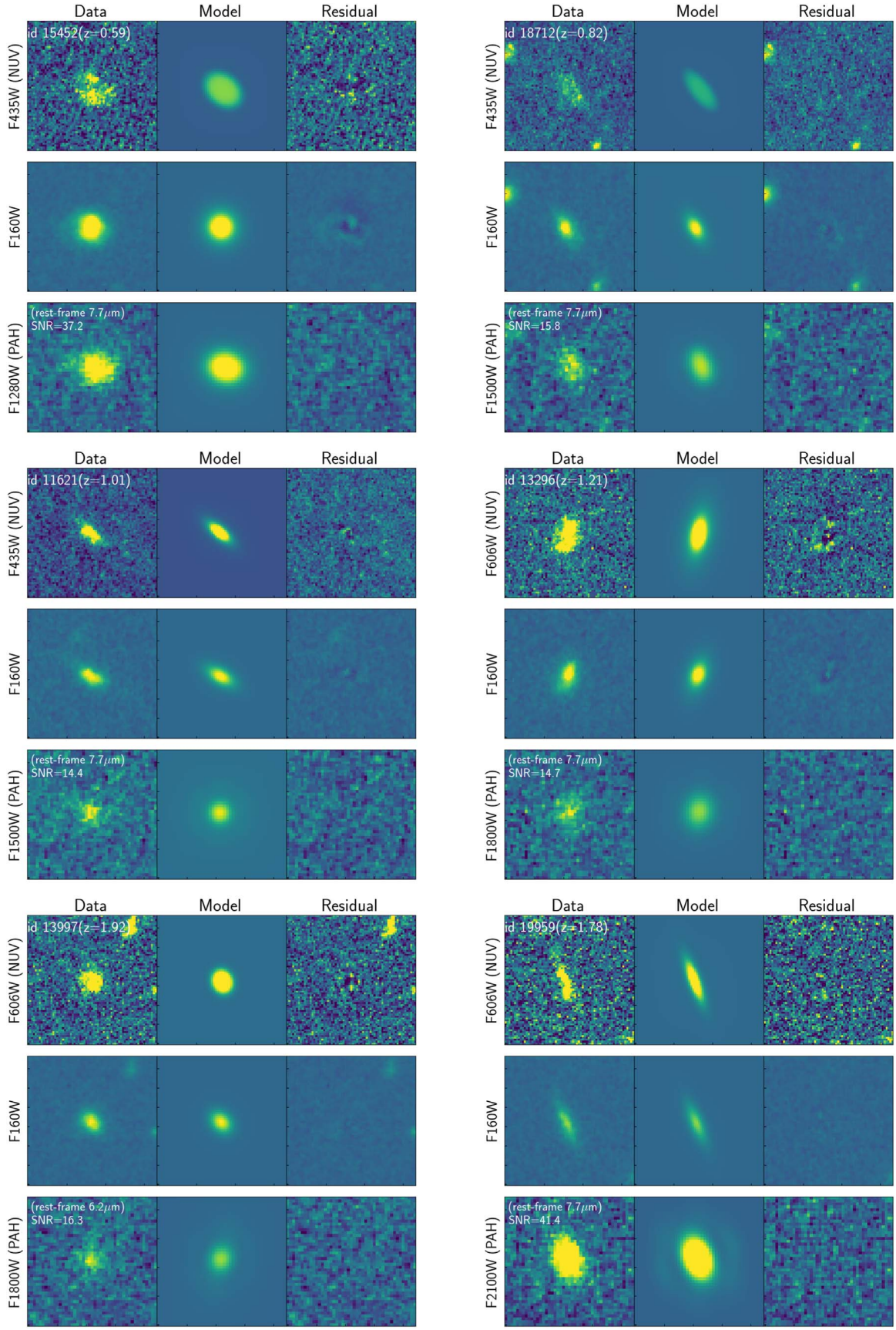

Figure 5. Examples of the GALFIT results. For each panel, from top to bottom, the plots show the GALFIT measurements in the NUV band, F160W, and PAH band. For each row, from left to right, are the data, GALFIT model (PSF-convolved), and residual. Each image is $2'' \times 2''$ centered on the target galaxies. For each galaxy, the ID and photometric redshift from Stefanon et al. (2017) are labeled. The S/Ns of MIRI fluxes are given in their panel.

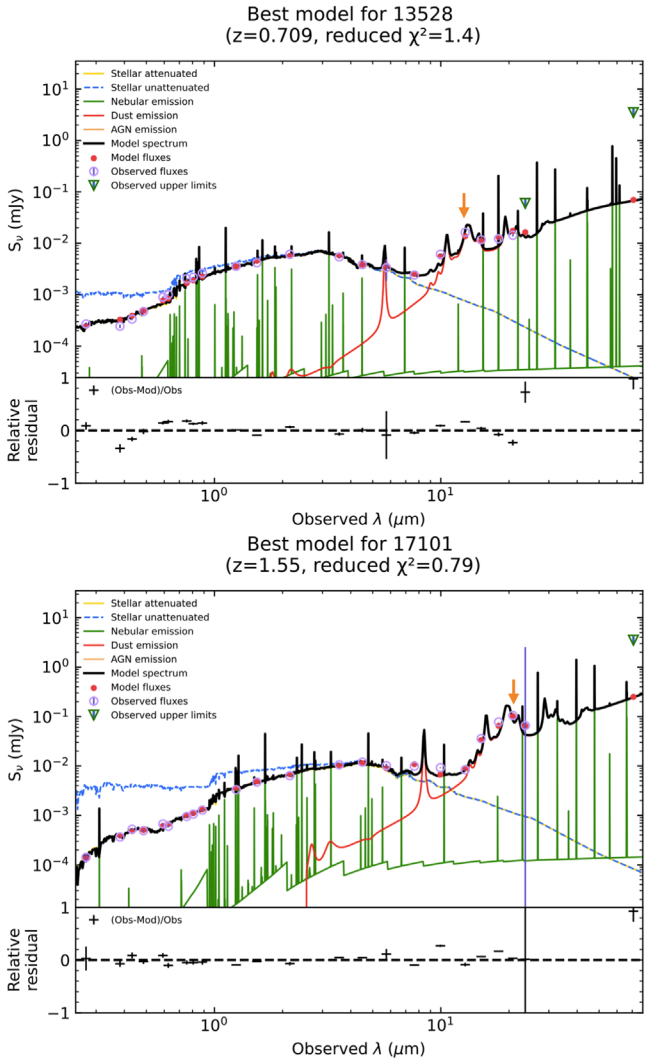

Figure 6. Examples of the best-fitting SED model from CIGALE. In each panel, the top shows the observed photometric fluxes with errors (purple), the 5σ upper limit fluxes (green triangles), the CIGALE-derived best model photometry (red dots), and the best-fitting CIGALE model (black). The best-fitting CIGALE model is the sum of the contributions from a dust attenuated stellar emission (yellow; the intrinsic stellar emission is indicated in blue), nebular emission (green), and dust emission (red). The bottom shows the fractional discrepancies between the model and the photometry. The reduced χ^2 of the best-fitting models are indicated in the top labels. The data for the PAH band are indicated by an orange arrow. In both examples shown here, the PAH band contains the rest-frame 7.7 μm features.

AGN to the total IR luminosity. We found six galaxies that likely host AGN based on these criteria. They have a median AGN fraction of 0.20 and an AGN fraction in the range of 0.17–0.32. We removed these galaxies in our final sample to exclude any possible effect due to AGN contamination.

We observe that the average effective radius in the PAH band of these AGN candidates is smaller than that in the F160W (their stellar continuum). The difference between these two is larger than that for our final sample (that excludes AGN candidates). This appears to imply that the presence of an AGN can reduce the measured galaxy sizes, leading to biased conclusions about the morphology of galaxies in the PAH bands. However, because our sample includes only a small number of these AGN candidates, adding them to our sample would not affect the average effective radii of the final sample nor impact our conclusions. We plan to explore the difference in MIRI morphology of AGN and non-AGN in the future with a larger sample.

3.5. Surface Density of the Stellar Mass and the SFR

We further use the morphology parameters measured from GALFIT to derive surface densities of stellar mass and SFR in our analyses to support the comparison between unobscured SFR, obscured SFR, and stellar mass. The surface density of stellar mass within effective radius ($\Sigma_{\rm eff}$) and within 1 kpc ($\Sigma_{1\ \rm kpc}$) are calculated following Cheung et al. (2012), Barro et al. (2017), and Matharu et al. (2022) as

$$\Sigma_{{\rm eff},M_*} = \frac{0.5M_*}{\pi R_{\rm eff}^2}, \tag{2}$$

$$\Sigma_{1\ {\rm kpc},M_*} = M_* \times f_{1\ \rm kpc}, \tag{3}$$

where M_* is the stellar mass, $R_{\rm eff}$ is the effective radius, and $f_{1\ \rm kpc}$ is the fraction of light contained within 1 kpc defined in Equation (1) both measured in F160W. An advantage of using $\Sigma_{1\ \rm kpc}$ is that it is more robust against the covariance between the effective size and Sérsic index, because the $\Sigma_{1\ \rm kpc}$ is the integral over the surface brightness (see, e.g., the discussion in Estrada-Carpenter et al. 2020; Matharu et al. 2022).

We convert the IR and FUV luminosities from CIGALEto SFR using calibrations from the literature for the UV SFR ($\rm SFR_{UV}$) and IR SFR ($\rm SFR_{IR}$) following Kennicutt & Evans (2012):

$${\rm SFR_{IR}} = \mathcal{K}_{\rm IR} \times \mathcal{L}_{\rm IR}, \tag{4}$$

$${\rm SFR_{UV}} = \mathcal{K}_{\rm UV} \times \mathcal{L}_{\rm FUV}, \tag{5}$$

where we adopt $\mathcal{K}_{\rm IR} = 10^{-43.41} M_\odot\ {\rm yr^{-1}\,erg^{-1}\,s}$ and $\mathcal{K}_{\rm UV} = 10^{-43.35} M_\odot\ {\rm yr^{-1}\,erg^{-1}\,s}$ (Madau & Dickinson 2014). As noted in Kennicutt & Evans (2012), these constants are appropriate for a Chabrier IMF.

We then calculate the $\Sigma_{\rm eff,SFR}$ and $\Sigma_{1\ \rm kpc,SFR}$ as

$$\Sigma_{\rm eff,SFR} = \frac{0.5 \times {\rm SFR}}{\pi R_{\rm eff}^2}, \tag{6}$$

$$\Sigma_{1\ \rm kpc,SFR} = {\rm SFR} \times f_{1\ \rm kpc}, \tag{7}$$

where we use the UV-based SFR with the $R_{\rm eff}$ and $f_{1\ \rm kpc}$ measured in the NUV band, and the IR-based SFR with the $R_{\rm eff}$ and $f_{1\ \rm kpc}$ measured in the PAH band to obtain their respective surface densities. We note that the UV-based SFR is uncorrected for dust attenuation, and therefore it represents the dust-unobscured portion of the galaxies' star formation.

4. Results

In this section, we first explore differences among morphologies measured in NUV band, PAH band, and F160W. We focus on the effective radius, Sérsic index, and fraction of light contained within 1 kpc in order to compare the spatial extent, the shape of light profile, and the concentration of different tracers of the light (of the unobscured star-forming regions, stellar continuum, and obscured star-forming regions, respectively). We compare the effective radius and Sérsic index of these three bands for MIRI-detected SFGs in Sections 4.1 and 4.2, respectively. In Section 4.3, we present the differences of the effective radius, Sérsic index, and fraction of light

contained within 1 kpc between the PAH band, NUV band, and F160W as a function of the stellar mass.

Second, we explore the surface density of obscured and unobscured SFRs (within the effective radius and within 1 kpc) and the obscured fraction of star formation in the center of galaxies. In Section 4.4, we compare the surface density of obscured SFR derived from SFR_{IR} and PAH-band morphology with the surface density of unobscured SFR derived from SFR_{UV} and NUV-band morphology and the surface density of stellar mass derived from M_* and F160W morphology. The comparison between the obscured fractions of star formation within 1 kpc and the integrated one over the entire galaxy are further present in Section 4.5.

4.1. On the Effective Radii of MIRI-detected SFGs

The left panels of Figure 7 show the effective radius histograms of the NUV and PAH bands and F160W and scatter plots of NUV/PAH-band versus F160W for the final sample of MIRI-detected SFGs. To account for the uncertainties in each measured morphological properties, we adopt a bootstrap method. For each bootstrap iteration, we randomly draw, with replacement, the same number of galaxies from the final sample, and for each galaxy, we randomly sample a mock value from a Gaussian with the measured value as the mean and the one-half of the difference between the 16th and 84th percentiles of as the standard deviation. We then obtain the median from the distribution of the bootstraped values. We repeat this process for 1000 iterations. We adopt the median and the 16th/84th percentiles of these bootstrap median values as the final median and associated errors. The medians of the effective radius and errors on the median are marked by arrows and shaded regions in the top panel and by large open markers with error bars in the bottom panel.

The median $R_{\rm eff}$ of the NUV band, F160W, and PAH band are 3.2 ± 0.4 kpc, 2.8 ± 0.3 kpc, and 2.7 ± 0.2 kpc, respectively (also see Table 2). It appears that the PAH-band sizes are, on average, similar to the F160W sizes, but they are both smaller than the NUV-band sizes.

We employed the Kolmogorov–Smirnov statistic (KS) test and Mann–Whitney U (MWU) test and their resultant p-values to determine a likelihood that the NUV band, PAH band, and F160 size distributions are consistent with the same parent distribution. We adopt a p-value $= 0.05$ as the significance threshold.[36] Both the KS and MWU statistics calculate a probability that two distributions are drawn from the same distribution. The MWU test is more sensitive to differences in medians, while the KS test is more sensitive to differences in the cumulative distributions of the two samples. The p-values of the KS and MWU tests on the $R_{\rm eff}$ distributions between each two bands are summarized in Table 4. The p-values on the same pair of bands between these two tests are mostly consistent.

Both tests return p-values $\leqslant 0.05$ between the $R_{\rm eff}$ distributions of the PAH and NUV bands. We therefore reject the null hypothesis that the spatial extent of obscured and unobscured star formation are drawn from the same parent distribution. However, the KS and MWU tests between the F160W sizes and the star formation ones are inconclusive: based on these tests, there is no significant difference between the $R_{\rm eff}$ distributions of the NUV and stellar continuum bands, nor between the PAH and stellar continuum bands. Therefore, we reject the null hypothesis that the NUV- and PAH-band sizes come from the same distribution, but we cannot rule out that this is the case for the PAH/NUV-band and F160W sizes.

[36] If the p-value < 0.05, the probability of the two distributions drawing from the same distribution is very small. Otherwise, we cannot reject the null hypothesis that the two distributions are drawn from the same distribution.

4.2. On the Sérsic Indexes of MIRI-detected SFGs

In the right panels of Figure 7, we show the Sérsic index histograms of the NUV band, PAH band, and F160W, and scatter plots of the NUV/PAH band versus F160W. The Sérsic indexes of F160W are, on average, larger than those of the NUV and PAH bands. The median Sérsic indexes of the NUV band, F160W, and PAH band are 0.8 ± 0.1, 1.1 ± 0.1, and 0.6 ± 0.1, respectively (also listed in Table 2). These median values suggest that the stellar continuum prefer a disk-like morphology ($n \sim 1$; and this is explored further by B. Magnelli et al. 2023, in preparation). In contrast, the obscured star formation (PAH band) and unobscured star formation (NUV band) profiles prefer a surface brightness profile that is flatter within the effective radius (this is implied by the lower Sérsic indexes).

In addition, the KS and MNU tests reveal that the Sérsic index distribution of F160W is significantly different from those of the PAH and NUV bands, while the Sérsic index distributions of the NUV and PAH bands are likely drawn from the same parent distribution. We interpret this as evidence that the obscured and unobscured star formation follow a profile with similar shape, which is different from the profile of the stellar continuum. We discuss this further below.

4.3. On the Mass–Morphology Relation of MIRI-detected SFGs

Previous studies have measured the size evolution of SFGs in their effective radii (i.e., in the stellar continuum band $R_{\rm eff} \propto (1+z)^{-0.75}$; see van der Wel et al. 2014). We therefore separate our MIRI-detected SFGs into a low-redshift subsample ($z \leqslant 1.2$) and a high-redshift subsample ($z > 1.2$). In Figure 8, we plot the effective radii of galaxies measured from their NUV band, PAH band, and F160W as a function of their stellar mass (as blue, red, and orange data points for the three bands, as labeled, with solid makers denoting the low-redshift subsample and open markers denoting the high-redshift subsample). Each subsample is then binned by stellar mass to show the average difference between these bands. The low/high-redshift subsample selection and binning are chosen to have a similar number of galaxies ($\sim$15) in each bin. The median effective radius and stellar mass and associated errors obtained from the bootstrap method (see Section 4.1) are shown as larger markers with error bars in the same color convention as data points for individual measurements. The median properties of galaxies in each subsample and mass bin are listed in Table 5.

The stellar size–mass relation for late-type galaxies at a rest-frame wavelength of $\sim$5000 Å from van der Wel et al. (2014) is shown as the light and dark gray shaded regions in redshift ranges of $z = 0.25$–1.25 and $z = 1.25$–2.25, respectively. The median sizes derived from the F160W band are consistent with the size–mass relations from van der Wel et al. (2014) for both low-redshift and high-redshift subsamples. We notice that our median F160W size of the high-mass bin for the high-redshift subsample is slightly offset from the size–mass relations,

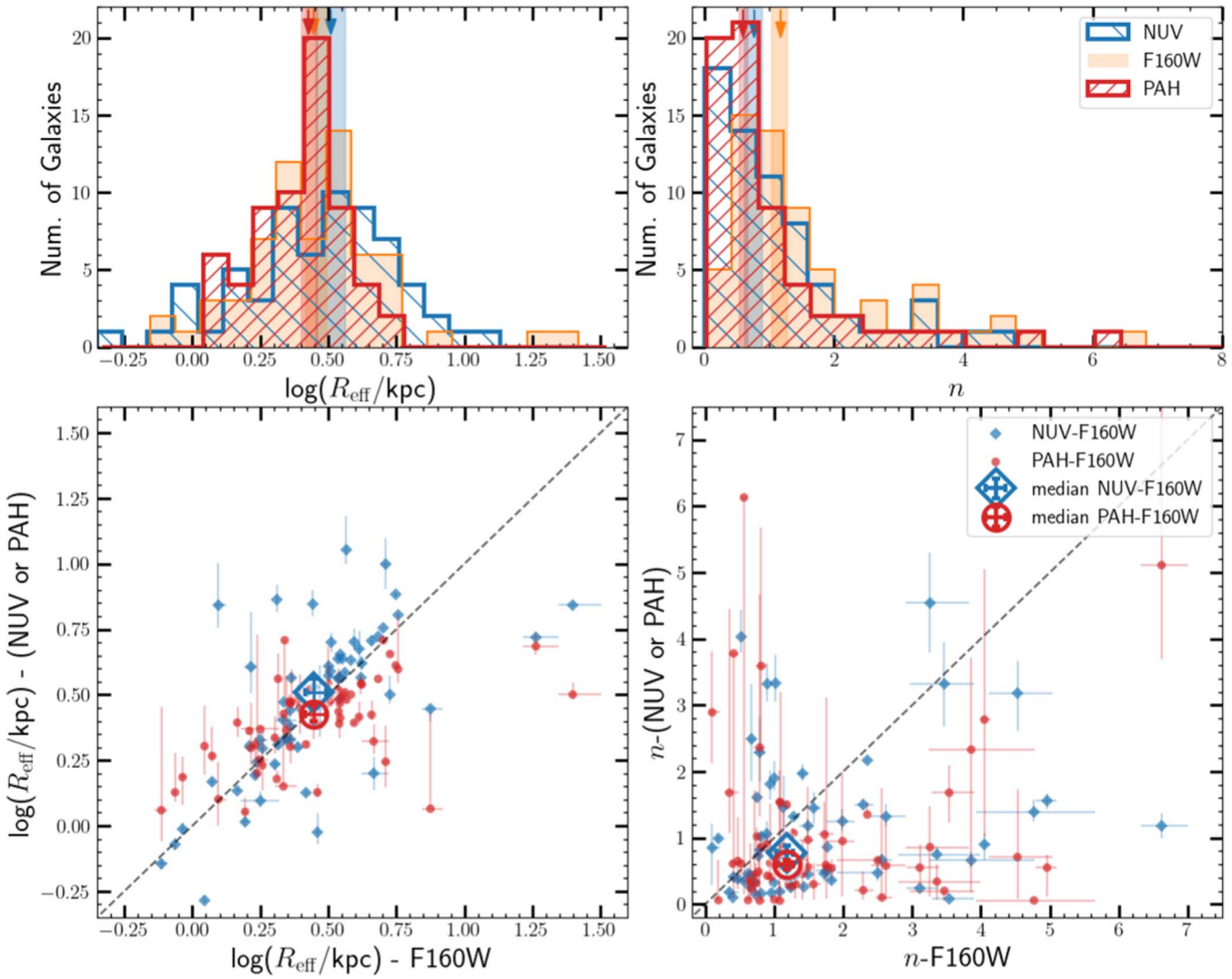

Figure 7. Top:Effective radius ($R_{\rm eff}$, left) and Sérsic index (n, right) histograms of the NUV band (blue), F160W (orange), and PAH band (red) for the final sample of MIRI-detected SFGs. Median values and associated uncertainties of these three bands are marked by arrows and shaded regions in the same color as their histograms. Bottom: $R_{\rm eff}$ (left) and n (right) of the NUV band (blue diamonds) and PAH band (red dots) vs. F160W. Median values and uncertainties are marked by large open markers with error bars in the same color as data points.

Table 3
Properties of Samples

Band (1)	$\langle z \rangle$ (2)	$\langle \log(M_*/M_\odot) \rangle$ (3)	$\langle R_{\rm eff}/{\rm kpc} \rangle$ (4)	$\langle n \rangle$ (5)
PAH	$1.2^{+0.6}_{-0.5}$	$9.7^{+0.3}_{-0.5}$	2.7 ± 0.2	0.6 ± 0.1
F160W			2.8 ± 0.2	1.1 ± 0.1
NUV			3.2 ± 0.4	0.8 ± 0.1

Note. (1) Name of band; (2),(3) median and 16th/84th percentiles of redshift and stellar mass of the final sample; (4),(5) median and uncertainties in median of effective radius and Sérsic index measured in each band using the bootstrap method.

Table 4
P-values from Statistic Tests

Comparison Bands (1)	$R_{\rm eff}$ KS (2)	$R_{\rm eff}$ MWU (3)	n KS (4)	n MWU (5)
PAH vs. F160W	0.09 (0.22)	0.22	10^{-5} (0.44)	10^{-5}
PAH vs. NUV	10^{-3} (0.36)	0.03	0.42 (0.16)	0.35
F160W vs. NUV	0.21 (0.19)	0.38	10^{-3} (0.31)	10^{-3}

Note. (1) Name of two tested bands. (2),(4) p-values from KS tests; the KS statistics are shown in the parentheses. (3),(5) p-values from Mann–Whitney U (MWU) tests. We adopt a p-value < 0.05 as rejecting the hypothesis that the two distributions are drawn from the same distribution.

though it is consistent within its uncertainty. This could suggest the galaxies sample is slightly biased in this mass bin toward galaxies with smaller sizes measured in their stellar continuum, but this would need to be confirmed with larger samples. We also warn the reader that this size–mass relation (and following morphology–mass relations) are based on a single redshift/mass binning that does not account for uncertainties on the stellar mass, redshift, and sample incompleteness. We will discuss this further in Section 5.2.

However, we see that the $R_{\rm eff}$–mass relation for the PAH and NUV bands show different evolution compared to the size–mass relations for the F160W and from van der Wel et al. (2014), especially for the low-redshift subsample. We further investigate the morphological difference of the PAH and NUV

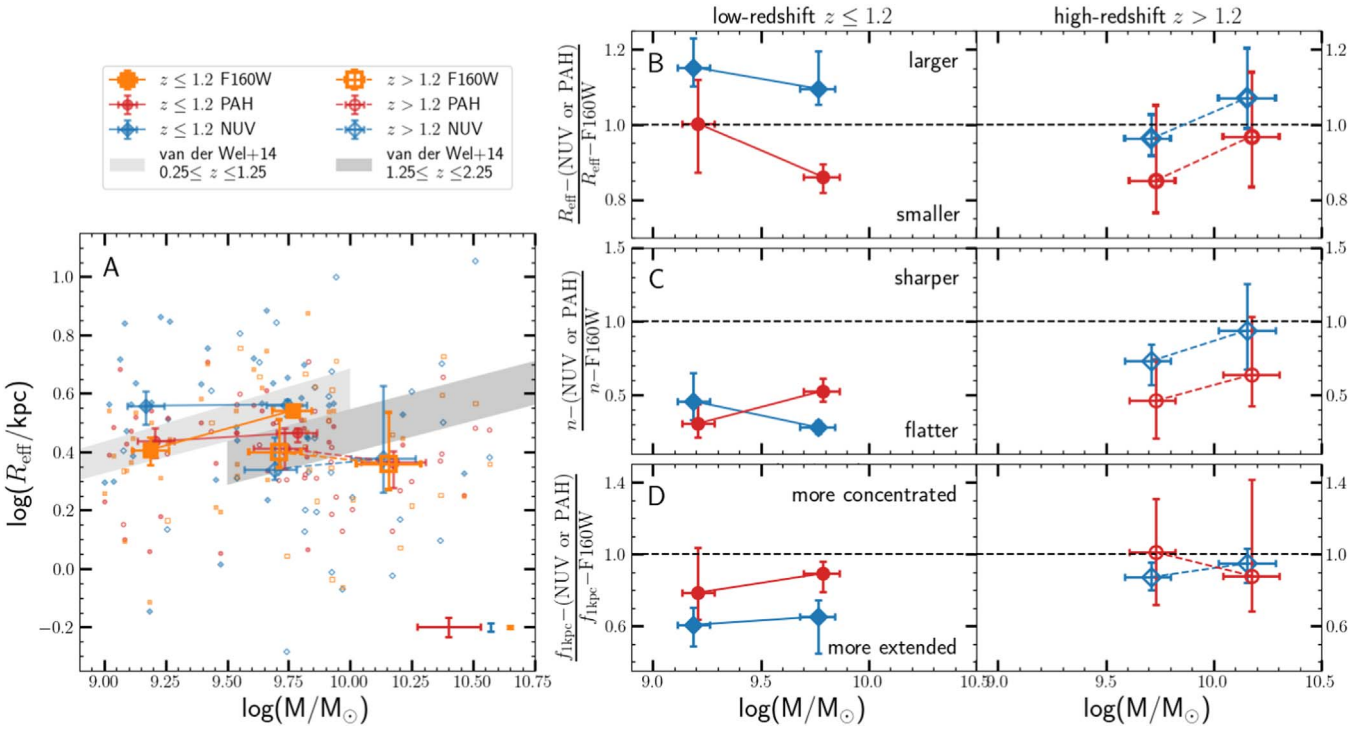

Figure 8. Morphological measurements vs. stellar mass for the final sample of MIRI-detected SFGs. Left: the effective radius–mass relation with the size measured in the NUV band (blue), F160W (green), and PAH band (orange). The larger colored data points with error bars show the median values and associated uncertainties obtained from the bootstrap method (Section 4.1). The solid makers denote the low-redshift ($z \leqslant 1.2$) subsample, and open markers denote the high-redshift ($z > 1.2$) subsample. The median of $R_{\rm eff}$ uncertainties of the three bands are indicated by colored error bars, as well as the median of stellar mass uncertainty. Right: the top, middle, and bottom panels show the ratio of the effective radius, Sérsic index, and $f_{1\ {\rm kpc}}$ measured in the NUV or PAH bands to the same quantity in the F160W band in bins of the stellar mass, separated into low-redshift and high-redshift subsamples. We shifted median values slightly along the x-axis in each panel for clarity.

bands relative to F160W as a function of the stellar mass, in terms of the effective radius in Section 4.3.1, Sérsic index in Section 4.3.2, and fraction of light contained within 1 kpc in Section 4.3.3.

4.3.1. The Size–Mass Relations

Figure 8 panel (B) compares the median ratio of sizes measured in the PAH and NUV bands to those in the F160W in bins of stellar mass. The sizes of obscured and unobscured star formation show different relations to the size of the stellar continuum (measured by the F160W band). In particular, at all masses, the median PAH/F160W size ratio is similar to or *smaller* than unity, while the median NUV/F160W size ratio is similar to or *larger* than unity.

For the low-redshift subsample, the median PAH-band size is similar to the F160W size in the low-mass bin, but the median PAH-band size is smaller than that of F160W in the high-mass bin with a 4σ significant level. For the high-redshift subsample, the median PAH-band sizes are not significantly different from the F160W sizes in either of the stellar mass bins: the differences between the sizes in the difference bands are within their uncertainties in both mass bins.

We also observed that at fixed *stellar mass* of $\log(M_*/M_\odot) = 9.5$–10 across the two redshift subsamples (i.e., the high-mass bin of the low-redshift subsample and the low-mass bin of the high-redshift subsample), the ratio of the sizes in the PAH band to F160W is $\sim$0.9 (see Figure 8). For galaxies at lower stellar mass ($\log(M_*/M_\odot) = 9$–9.5), this ratio is unity. Despite the large errors on these ratios, these results tentatively suggest that, as galaxies increase their stellar mass, the extent of the obscured star formation, traced by the PAH band, decreases. We discuss this further in Section 5.3.

On the other hand, the NUV-band sizes are larger than the F160W sizes for both stellar mass bins for the low-redshift subsample. This is significant at 2σ for the low-mass bin. The NUV sizes for the high-redshift subsample are similar to the F160W sizes (within 1σ uncertainties).

Assuming that dust attenuation is responsible for some of the differences, and if dust is concentrated at the center of galaxies, the observed effective radius of galaxies in the NUV bands and stellar continuum should be larger than their intrinsic effective radius (e.g., Nelson et al. 2016b). This could account for the modestly larger NUV sizes we find in the two higher mass bins of both redshift subsamples (Suess et al. 2019, 2021). However, the obscured fraction of star formation is relatively small in low-mass galaxies as compared to massive galaxies, indicating the amount of dust is lower in these low-mass galaxies (see more discussion in Section 4.5). Thus, the effect of dust cannot solely explain the much larger unobscured star formation at the lower-mass bin of the low-redshift subsample. We further discuss this in Section 4.4. Thus, for these low-mass galaxies, their star formation might be intrinsically larger than the stellar continuum.

4.3.2. The Sérsic Index–Mass Relations

The Sérsic index can inform the shape of profiles as a larger n corresponding to a sharper profile within the effective radius, while a smaller n corresponding to a flatter profile within the effective radius. We compare the median ratios of the Sérsic indexes measured in the PAH and NUV bands to those in the F160W in bins of stellar mass in panel (C) of Figure 8. The

Table 5
Median Properties of Galaxies in each Subsample/Bin as Shown in Figure 8

Subsample	Mass Bin	Num. of Gals	$\langle z \rangle$	$\langle \log(M_*/M_\odot) \rangle$	PAH Band		NUV Band		F160W	
					$\langle R_{\rm eff} \rangle$ (kpc)	$\langle n \rangle$	$\langle R_{\rm eff} \rangle$ (kpc)	$\langle n \rangle$	$\langle R_{\rm eff} \rangle$ (kpc)	$\langle n \rangle$
(1)	$\log(M_*/M_\odot)$ (2)	(3)	(4)	(5)	(6)	(7)	(8)	(9)	(10)	(11)
$z \leqslant 1.2$	<9.5	18	0.7 ± 0.1	9.2 ± 0.1	2.7 ± 0.3	0.5 ± 0.2	3.6 ± 0.5	0.6 ± 0.2	2.6 ± 0.3	1.1 ± 0.1
	⩾9.5	16	0.7 ± 0.1	9.8 ± 0.1	2.9 ± 0.2	0.6 ± 0.1	3.6 ± 0.2	0.4 ± 0.2	3.5 ± 0.1	1.3 ± 0.2
$z > 1.2$	<9.9	15	1.4 ± 0.5	9.7 ± 0.1	2.6 ± 0.4	0.7 ± 0.4	2.2 ± 0.4	0.8 ± 0.1	2.5 ± 0.5	1.4 ± 0.8
	⩾9.9	15	2.0 ± 0.6	10.2 ± 0.1	2.3 ± 0.3	0.6 ± 0.2	2.4 ± 1.0	1.2 ± 0.3	2.3 ± 0.7	1.0 ± 0.2

Note. (1) Redshift cut of each subsample; (2) stellar mass range of mass bin; (3) number of galaxies in each mass bin; (4),(5) median and associated uncertainties of the redshift and stellar mass for each bin; (6)–(11) median and associated errors of $R_{\rm eff}$ and n in the PAH band, NUV band, and F160W for each bin. The median values are obtained from the bootstrap method that also account for uncertainties on morphologies. The errors are the one-half of the difference between the 16th and 84th percentiles of the bootstrap median values.

Sérsic indexes measured in the PAH band are consistently smaller than those of F160W across the stellar mass range and for both high-redshift and low-redshift subsamples. This indicates that the surface brightness profiles of obscured star formation are generally flatter than those of stellar continuum (at least within the effective radius). As illustrated in Figure 7, the fact that the average Sérsic index of galaxies in the PAH band are $n \simeq 0.6$, which indicates that the PAH emission follows profiles that are flatter than those of the stellar continuum with an average $n \simeq 1.2$, which may trace both disk and bulge components.

Similarly, the median Sérsic indexes measured in the NUV band for the low-redshift subsample are smaller than those of F160W and largely consistent with those measured in the PAH band. This result suggests that for galaxies at $z \leqslant 1.2$, the profiles of the obscured and unobscured star formation in these galaxies follow a similar shape. However, the median ratios of the Sérsic index measured in the NUV band to those in the F160W for the high-redshift subsample are closer to unity, which suggests there might be a redshift evolution in the morphological profiles in these different wavelengths or other bias (see next section).

4.3.3. The $f_{1\ kpc}$–Mass Relations

Finally, we compare the fraction of light contained within 1 kpc measured in the PAH and NUV bands relative to that of F160W ($f_{1\ \rm kpc}$ using Equation (1)). As shown in panel (D) of Figure 8, the median ratios of $f_{1\ \rm kpc}$ of the PAH band to the F160W band is close to unity (within their uncertainties). This is true at all redshifts and stellar masses. This suggests that the concentration of obscured star formation and the stellar light are similar.

However, the median $f_{1\ \rm kpc}$ measured in the NUV band is significantly smaller than those measured in the F160W band for the low-redshift subsample at the 3σ and 2σ significant levels, suggesting that the unobscured star formation is more extended than the stellar continuum. The median ratios of $f_{1\ \rm kpc}$ of the NUV band to F160W is closer to unity for the high-redshift subsample, implying that there is either real redshift evolution or some bias in our choice of bandpasses at the different redshifts.

Combining the differences in the NUV-band morphologies (i.e., $R_{\rm eff}$, n, and $f_{1\ \rm kpc}$) between the low-redshift and high-redshift subsamples, we suspect that our NUV morphology measurements are dominated by the clumps for these high-redshift galaxies or massive galaxies, possibly due to their high dust attenuation, rather than the full extend of unobscured star formation for those low-redshift galaxies or low-mass galaxies. However, due to the small sample size and the incomplete sample in the mass–redshift space, we cannot draw a conclusion on whether this effect is a mass dependence or due to evolution. However, this could also be due to some bias in our choice of bandpasses at the different redshifts. At $z \sim 1.1$, the NUV band refers to rest-frame wavelengths of 0.21 μm, while the stellar continuum refers to 0.76 μm. However at $z \sim 2.5$, the NUV band refers to rest-frame wavelengths of 0.17 μm, while the stellar continuum refers to 0.45 μm. This could in part explain why the stellar continuum morphology appears to be similar to the NUV-band morphology in the high-mass, high-redshift bin.

4.4. The Surface Density–Mass Relations

In this section, we compare the surface density of SFR derived from IR and UV and the surface density of the stellar mass, as shown in Figure 9. To better quantify the relations, we plot $\Sigma_{\rm SFR_{IR}}$, $\Sigma_{\rm SFR_{UV}}$, and Σ_{M_*} together. However, $\Sigma_{\rm SFR}$ (UV and IR values) and Σ_{M_*} are plotted in relative units (i.e., the y-axis zero-point is offset between $\Sigma_{\rm SFR}$ and Σ_{M_*}). However, the SFR and stellar-mass surface densities span the same range in the logarithm space so the *slope* of the relation between the surface density and stellar mass can be directly compared. Previous studies have found that the slopes of the correlation between $\Sigma_{\rm eff,M_*}$ and $\Sigma_{\rm 1\ kpc,M_*}$ and the stellar mass are not redshift dependent at $0.5 < z < 3$, but the intercepts of these correlations change with the redshift (e.g., Barro et al. 2017). Thus, we plot low- and high-redshift subsamples separately.

We see clear correlations between the stellar mass and the surface density of the stellar mass, and between the stellar mass and the surface density of the IR-based SFRs. However, we see that the surface density of UV-based SFRs remain relatively constant with the stellar mass. This is true both for $\Sigma_{\rm eff}$ and $\Sigma_{\rm 1\ kpc}$. A reminder that UV-based SFRs is not corrected for dust attenuation (see Section 3.5). To constrain these relations, we fit a linear relation between each surface density and stellar mass using a Gaussian mixture model (linmix; Kelly 2007). The best-fitted parameters are the median of 400 fitted parameters of random draws from the posterior, and the associated errors are one-half of the difference between the 16th and 84th percentiles of the fitted parameters. This best-fitted lines are shown in Figure 9, along with 400 random

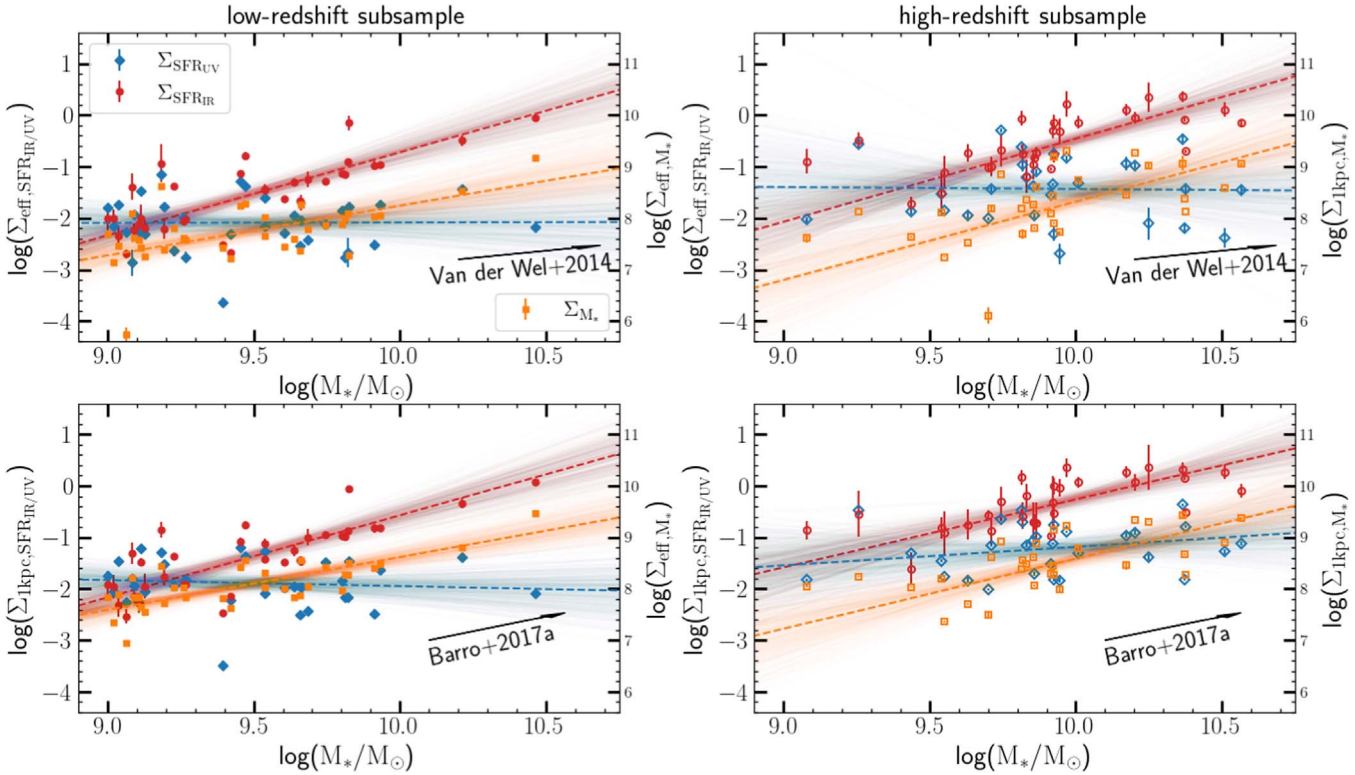

Figure 9. Surface density within the effective radius ($\Sigma_{\rm eff}$, top) and within 1 kpc ($\Sigma_{1\ \rm kpc}$, bottom) of $\rm SFR_{IR}$, $\rm SFR_{UV}$, and stellar mass as functions of the stellar mass, and separated into low-redshift (left) and high-redshift (right) subsamples. In each panel, the small colored data points are the measurements for individual galaxies. The dashed color lines are best-fitted linear relations, along with 400 randoms fits from the posterior. The black arrows are the mean growth from the literature (van der Wel et al. 2014; Barro et al. 2017). Note that the zero points of the ordinates for the surface density of the SFR and surface density of the stellar mass are different. However, these ordinates span the same range for both surface densities ($\Sigma_{\rm SFR}$ and Σ_{M_*}). Therefore, the slope of these relations can be directly compared but not the absolute values.

Table 6
Fits of the Surface Density of Stellar Mass, IR-based and UV-based SFRs–Mass Relations in the Form of $\log\Sigma = \alpha(\log(M_*/M_\odot) - 9) + \log(A)$

Σ-mass	Subsample	$\Sigma_{\rm SFR_{IR}}$		$\Sigma_{\rm SFR_{UV}}$		Σ_*	
		α	$\log(A)$	α	$\log(A)$	α	$\log(A)$
(1)	(2)	(3)	(4)	(5)	(6)	(7)	(8)
$\Sigma_{\rm eff}$	low-z	1.6 ± 0.3	-2.3 ± 0.2	0.0 ± 0.3	-2.1 ± 0.2	1.0 ± 0.3	7.3 ± 0.2
	high-z	1.6 ± 0.3	-2.1 ± 0.3	-0.0 ± 0.5	-1.4 ± 0.5	1.5 ± 0.5	6.8 ± 0.5
$\Sigma_{1\ \rm kpc}$	low-z	1.5 ± 0.5	-2.2 ± 0.2	-0.1 ± 0.3	-1.8 ± 0.2	1.0 ± 0.2	7.6 ± 0.1
	high-z	1.3 ± 0.3	-1.6 ± 0.3	0.4 ± 0.4	-1.5 ± 0.4	1.4 ± 0.4	7.2 ± 0.4

Note. (1) Name of Σ within the effective radius or within 1 kpc; (2) name of subsample; (3)–(8) slopes and intercepts of the fitted Σ–mass relations using linmix (Kelly 2007). The best-fitted parameters are the median of 400 fitted parameters of random draws from the posterior, and the associated errors are one-half of the difference between the 16th and 84th percentiles of the fitted parameters.

draws from the posterior. The slopes of these fitted lines and associated errors are listed in Table 6.

The Σ_{M_*}–stellar mass relations derived from the literature are indicated by black arrows in Figure 9. It is worth noting that the stellar mass and stellar mass surface density are not independent. In the top panel of Figure 9, the black arrow shows the mean size–stellar mass relation, $\Delta\log(r_e) = 0.22\Delta\log(M_*)$, from van der Wel et al. (2014), which gives the surface density of the stellar mass within the effective radius growth as $\Delta\log(\Sigma_{M_*}) = 0.56\Delta\log(M_*)$. This is consistent with $\Delta\log(\Sigma_{M_*}) = 0.60\pm 0.05\Delta\log(M_*)$ from Barro et al. (2017). Our best-fit slope of $\Sigma_{\rm eff,M_*}$ at $z < 1.2$ is slightly larger than these relations from the literature but only at $\sim 1\sigma$ significant. However, the best-fit slope of $\Sigma_{\rm eff,M_*}$ at $z > 1.2$ is significantly larger than these relations. These are similar to the mass–size comparison, where the median F160W size of the high-mass bin for the high-redshift subsample is offset from the size–mass relations from van der Wel et al. (2014). In the bottom panel, the black arrow shows the $\Delta\log(\Sigma_{1\ \rm kpc}) = 0.9\Delta\log(M_*)$ from Barro et al. (2017). Our $\Sigma_{*,1\ \rm kpc}$–M_* relation at $z < 1.2$ is nearly identical to that found by Barro et al. (2017), and they are different for the high-redshift subsample.

It is interesting that, in both the $\Sigma_{\rm eff}$ and $\Sigma_{1\ \rm kpc}$ panels, $\Sigma_{\rm SFR_{IR}}$ increases much faster than $\Sigma_{\rm SFR_{UV}}$ for both the low- and high-redshift subsamples. The difference between $\Sigma_{\rm SFR_{IR}}$ and $\Sigma_{\rm SFR_{UV}}$ suggests that galaxies with higher stellar masses have a higher obscured fraction of star formation in their inner regions. We further explored the obscured fraction of star formation within

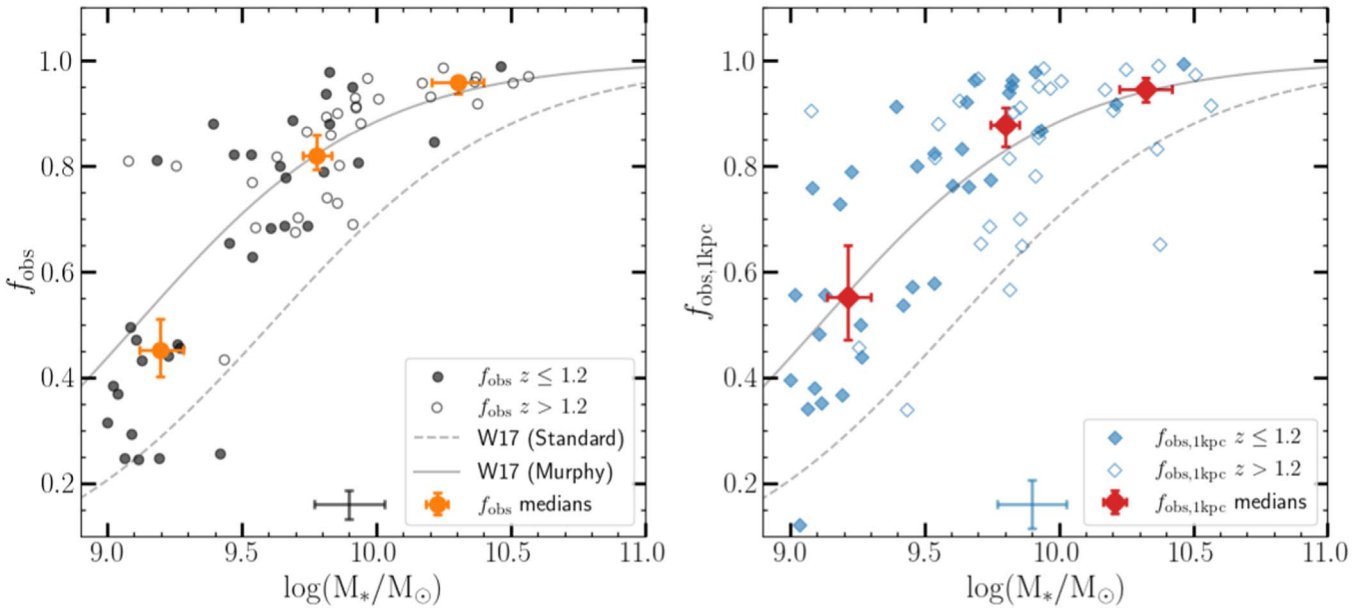

Figure 10. Obscured fraction of star formation as a function of the stellar mass integrated over the entire galaxy ($f_{\rm obs}$, left) and within 1 kpc ($f_{\rm obs,1\ kpc}$, right). Solid and open markers are used for galaxies at $z \leqslant 1.2$ and at $z > 1.2$, respectively. The larger orange and red data points with error bars show the median $f_{\rm obs}$ and median $f_{\rm obs,1\ kpc}$ vs. the median stellar mass and associated uncertainties. The median of errors on $f_{\rm obs}$, $f_{\rm obs,1\ kpc}$, and stellar mass are indicated by black and blue error bars in the bottom of both panels. The $f_{\rm obs}$ (measured on the whole galaxy)—mass relations for galaxies at $z \sim 0$–2.5 from Whitaker et al. (2017) are shown as the gray lines in both panels, though it is only a valid comparison to the $f_{\rm obs}$ in the left panel.

1 kpc as a function of the stellar mass and compare to that integrated over the entire galaxies in Section 4.5.

In addition, the $\Sigma_{\rm SFR_{IR}}$ increases with the mass slightly faster than the Σ_{M_*} for the low-redshift subsample. The steeper slope of $\Sigma_{\rm SFR_{IR}}$ is not likely due to differences in morphology because the $R_{\rm eff}$s of the PAH band are only slightly smaller than those in the F160W in massive galaxies. Moreover, the $f_{1\ \rm kpc}$ of the PAH band and F160W are largely consistent across the redshift and stellar mass ranges. Therefore, this steeper slope is most likely due to the increase in $\rm SFR_{IR}$ at higher masses. This result indicates that star-forming massive galaxies, at least at $z \leqslant 1.2$, experience a faster buildup of their dust content in their inner regions compared to their stellar mass. This result could be explained by the fact that more massive galaxies might be intrinsically more capable of dissipative gas accretion toward the center (e.g., Dekel et al. 2009; Dekel & Burkert 2014). However, the slopes of $\Sigma_{\rm SFR_{IR}}$ and Σ_{M_*} are similar for the high-redsfhit subsample. We suspect this is due to the lack of galaxies with stellar masses lower than $10^{9.5} M_\odot$, which seems to drive the $\Sigma_{\rm SFR_{IR}}$–mass correlation for the low-redshift subsample.

4.5. On the Fraction of Obscured Star Formation

Having estimated both the SFR derived from IR and UV and the SFR surface densities, we can further compare the obscured fraction of star formation integrated over the entire galaxy ($f_{\rm obs}$) and measured within 1 kpc ($f_{\rm obs,1\ kpc}$), defined as

$$f_{\rm obs} = \rm SFR_{IR}/(SFR_{IR} + SFR_{UV}), \quad (8)$$

$$f_{\rm obs,1\ kpc} = \Sigma_{\rm 1\ kpc,SFR_{IR}}/(\Sigma_{\rm 1\ kpc,SFR_{IR}} + \Sigma_{\rm 1\ kpc,SFR_{UV}}), \quad (9)$$

where $\rm SFR_{IR}$ and $\rm SFR_{UV}$ are the IR-based and UV-based SFRs; $\Sigma_{\rm 1\ kpc,SFR_{IR}}$ and $\Sigma_{\rm 1\ kpc,SFR_{UV}}$ are the surface densities of the IR-based and UV-based SFRs within 1 kpc (see Section 3.5). In Figure 10, we plot $f_{\rm obs}$ and $f_{\rm obs,1\ kpc}$ versus the stellar mass of individual galaxies and the median values in three equally spaced stellar mass bins. The medians and associated errors are obtained from the bootstrap method.

Meanwhile, we show the $f_{\rm obs}$–mass relations for galaxies at $z \sim 0$–2.5 from Whitaker et al. (2017) in gray lines as a reference to the relation between the obscured fraction integrated over the entire galaxy and stellar mass. Whitaker et al. (2017) used Spitzer MIPS 24 μm observations of a mass complete sample at $\log(M_*/M_\odot) \geqslant 9$ with two methods of SFR conversions ("standard" and "Murphy"). For the "standard" method, $\rm SFR_{IR}$ is derived by converting the 24 μm flux densities to the total IR luminosity based on Dale & Helou (2002) IR SED templates and adopt IR luminosity to $\rm SFR_{IR}$ following Kennicutt (1998), and $\rm SFR_{UV}$ is derived from rest-frame UV luminosity at 2800 Å based on Bell et al. (2005). For the "Murphy" method, $\rm SFR_{IR}$ and $\rm SFR_{UV}$ are derived from the 24 μm flux densities and rest-frame UV luminosity at 1500 Å, respectively, following Murphy et al. (2011). Our $f_{\rm obs}$ based on the MIRI and rest-frame FUV data favor the observed fractions in the standard conversion from Whitaker et al. (2017).

We observe a consistent strong mass dependence of the obscured fraction of star formation within 1 kpc and on the galaxy scale. The former relation has also been shown in Figure 9. At lower stellar masses $M_* \lesssim 10^{9.5} M_\odot$, the obscured fractions are lower ($\sim$0.45 for $f_{\rm obs}$ and $\sim$0.55 for $f_{\rm obs,1\ kpc}$) than those in more massive galaxies ($f_{\rm obs}$ and $f_{\rm obs,1\ kpc} \gtrsim 0.8$). Therefore, the NUV-band and F160W morphologies of low-mass galaxies should be less affected by dust attenuation, compared to these morphologies of more massive galaxies. This result further supports the assertion that dust attenuation is not a primary cause for the more extended Hα sizes with stellar mass $M_* \sim 10^{9.5} M_\odot$ at $0.5 \leqslant z \leqslant 1.7$ (e.g., Matharu et al. 2022). Rather this supports "inside-out" growth for galaxies in this mass and redshift range.

Furthermore, we notice that the median $f_{\rm obs,1\ kpc}$ of low-mass galaxies ($M_* \leqslant 10^{9.5} M_\odot$) is higher than the median $f_{\rm obs}$ by 10%, tentatively suggesting a higher obscured fraction of star

formation within 1 kpc in these low-mass galaxies. This could be explained by the more extended profile of the NUV band in low-mass galaxies at $z \leqslant 1.2$, which lower the surface density of $SFR_{UV,1\ kpc}$ and thus increase $f_{obs,1\ kpc}$.

5. Discussion

The JWST/MIRI data have enabled—for the first time—the ability to study the mid-IR morphologies of distant galaxies. This puts these studies on a similar footing as studies of the rest-frame UV and optical morphologies from HST. The comparisons of the morphological parameters derived from the JWST/MIRI data and HST/ACS and WFC3 data (effective radius, Sérsic index, fraction of light contained within 1 kpc) show differences in the physical distribution of stars (traced by the stellar continuum) and star formation (traced by the IR-based and UV-based star formation). These differences furthermore depend on the stellar mass and redshift. In particular, our analysis of the surface density of the IR-based SFR, UV-based SFR (and the ratio of the surface density of IR-based and UV-based SFR), and the stellar mass reveal that galaxies with higher stellar masses have particularly higher obscured SFRs.

In this section, we first test the robustness of the morphological measurements by considering the effect of the angular resolution of the data (Section 5.1) and discuss caveats associated with our results (Section 5.2). We then discuss the implications of our results on the spatially resolved star formation and on galaxy formation, compared to what was known from studies based on rest-frame optical/UV data only (Section 5.3).

5.1. The Robustness of the Morphology Measurements

There are known systematics that can impact the morphological measurements derived from fitting models to the galaxy surface brightness. The angular resolution of the image can limit our ability to measure accurate sizes and Sérsic indexes (e.g., Häussler et al. 2007). For galaxies with very compact morphologies (i.e., where R_{eff} is small compared to the PSF FWHM), the uncertainties in the size and Sérsic indexes are less robust and more degenerate. For galaxies in our sample this will have the most impact on the PAH-band morphologies as the JWST/MIRI images have a larger PSF FWHM compared to the HST/ACS and WFC3 data. However, we argue that this is not a significant factor on our results. The MIRI PSF has a $\sigma = \mathrm{FWHM}/2.35$ that ranges from 0.1 to 0.3 from 7.7 to 21 μm. Figure 7 shows that the majority of the PAH-band effective sizes are larger than 2 kpc, which corresponds to 0.″2–0.″3 over the redshift range of our sample. This is comparable to—or larger than—the PSF and implies that for the majority of our sample the morphologies are reasonably resolved (and the GALFIT results relatively robust).

Nevertheless, we also test the robustness of the morphology measurements by selecting galaxies with measurements of R_{eff} that are significantly larger than the PSF. For a Gaussian distribution, the R_{eff} of the PSF is 50% of its FWHM. Because morphologies are fitted with different Sérsic indexes, we then subdivide these galaxies into samples with $R_{eff}/\mathrm{FWHM} > 0.5$, 0.75, and 1 in all three of the NUV, F160W, and PAH bands. The median R_{eff}, n, and $f_{1\ kpc}$ ratios of the PAH and NUV bands to F160W for these subsamples are shown in Figure 11. The average differences between these morphologies of the PAH/NUV bands and F160W of the full sample and these subsamples remain unchanged. As we found above for the full sample, the PAH-band sizes are slightly smaller, with lower n, and similar $f_{1\ kpc}$ as F160W, and the NUV-band sizes are slightly larger, with lower n, and lower $f_{1\ kpc}$ compared to the values in the F160W band. Quantitatively, the R_{eff} and $f_{1\ kpc}$ of PAH band/F160W for galaxies with $R_{eff}/\mathrm{FWHM} > 1$ shift to a somewhat larger and more extended region. This is most likely due to a selection effect. We are preferentially selecting galaxies with larger PAH, because this PSF selection dominantly act on the PAH, given the relatively large PSF of MIRI image. We therefore conclude that the trends in the data are not driven by differences in the angular resolution of the different bands.

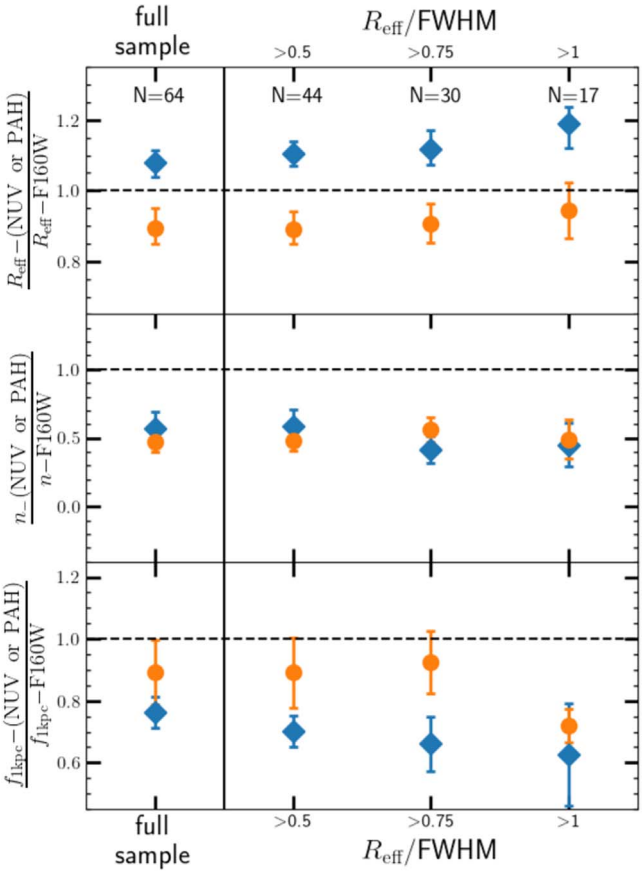

Figure 11. Tests of the effect of image resolution and AGN on the morphological parameter measurements. The left panel shows the ratio of the sizes, Sérsic indexes, and fraction of light contained within 1 kpc between the NUV and PAH bands against the F160W band for the full samples. The right panel shows the results when the sample is divided into galaxies where their sizes are greater than 0.5×, 0.75×, and 1.0× the PSF FWHM of all three bands (PAH and NUV bands and F160W). No differences are shown between the full sample and these subsamples; thus, the results of the morphological differences do not depend strongly on size.

5.2. Caveats

In this section, we discuss some caveats that might affect our results. First, our results on the morphology–stellar mass relations are based on a single redshift/mass binning that does not account for uncertainties in the stellar mass, redshift, and sample incompleteness. Our binning method is chosen to have a similar number of galaxies in each bin in order to increase the statistical power in each bin.

We have tested the effect of using different binning methods, but we find that these do not seriously impact our results. For the low-redshift subsample, if we bin galaxies into three bins of stellar mass, $\log(M_*/M_\odot) < 9.35$, ~9.35–9.70, and >9.70); then the median sizes of the PAH band remain ~10% smaller than those of F160W for galaxies in $\log(M_*/M_\odot) \sim 9.35$–9.70 and >9.70 at the 3.5σ and 2σ significant levels. Meanwhile, the median size of the NUV band remain ~10% larger than that of F160W for galaxies in $\log(M_*/M_\odot) \sim 9$–9.35 at a 2σ significant level. For the high-redshift subsample, if we bin galaxies into three bins in stellar mass, $\log(M_*/M_\odot) \sim$ 9.50–9.75, ~9.75–10, and >10, then we see larger errors on the median size ratios of the PAH band and NUV band to F160W, similar to Figure 8. Thus, using slightly different binning methods does not affect our main results significantly.

Regarding the sample incompleteness, we lack galaxies with high stellar mass at low redshift, mostly due to the small survey area. We used only two MIRI pointings that have UV coverage with UVCANDELS, which have a total area of $\lesssim$5 arcmin^2. We also are lacking galaxies with low stellar mass at high redshift, because they appear fainter in brightness and are excluded due to GALFIT failures. This restricts our sample to the stellar-mass range studied above. In addition, as mentioned in Section 3.2, our sample selection might bring a potential bias toward SFGs with moderate dust and against very dusty SFGs because of excluding NUV-undetected sources. Both of these potential biases will be rectified from a larger area and deeper imaging with future MIRI observations.

The second caveat is related to our estimate of the IR SFR. We use the mid-IR to anchor the total IR, which could lead to uncertainties in the total IR luminosity and IR SFR. We derive the total IR luminosities using CIGALE to model the full UV, optical, and IR SED and with fluxes span from UV to mid-IR (as presented in Section 3.4). These SED fitting include limits from Spitzer/MIPS (or in a few cases detections), which restricts the upper limit of IR luminosities. Nevertheless, the lack of longer wavelength data could lead to additional systematic uncertainties in our IR luminosities (Jin et al. 2018; Liu et al. 2018). This could be improved by stacking the MIRI-detected galaxies in the MIPS data, and also in Herschel Photodetector Array Camera and Spectrometer (PACS) and Spectral and Photometric Imaging Receiver (SPIRE) data that exist in these fields, which would improve the average relation between the mid-IR flux densities and the full shape of the far-IR SED. Such analysis is beyond the scope of this work, but we expect to pursue it in a future study.

5.3. Implications for Spatially Resolved Star Formation in Distant Galaxies

In this paper we have measured the morphologies of MIRI-detected SFGs in the rest-frame NUV, PAH emission, and stellar continuum. This allows us to account for where stars are forming as traced by the NUV and PAH emission, compared to where they have formed, as traced by the stellar continuum. Here we interpret these results in terms of how galaxies grow with time.

First, it is interesting that the Sérsic indexes derived from the PAH emission and NUV-band data favor exponential disks, or shallower profiles, with $n \lesssim 1$. In contrast the Sérsic indexes of the stellar continuum traced by the F160W data favor slightly larger values, with $n \gtrsim 1$. One interpretation from this is that star formation proceeds in a disk-like fashion. The stellar continuum, which is the integral of the history of star formation, shows that star formation must have first occurred in the central regions, with higher densities (Σ_*), and subsequently quenched such that the profile of the stellar mass remains more concentrated than the ongoing star formation.

Second, we consider the size evolution, where our analysis of the NUV-band morphologies suggests that unobscured star formation sizes are larger and more extended than the stellar continuum. At first glance, this is consistent with results measured from Hα at $z \sim 0.5$–3 (Nelson et al. 2016a; Wilman et al. 2020; Matharu et al. 2022). These earlier studies found that the sizes of the Hα emission exceed that of the stellar continuum suggesting ongoing star formation activity at preferentially larger radii than existing stars (i.e., galaxies are forming "inside-out"). Although, these studies may be impacted by effects of dust attenuation (e.g., Nelson et al. 2016b).

It is instructive to compare the results on the Hα and NUV sizes of galaxies. Matharu et al. (2022) found that the mean Hα effective radius is 1.2 ± 0.1 times larger than that of the stellar continuum for SFGs with $9.25 < \log(M_*/M_\odot) < 9.70$ in the redshift range $0.5 \lesssim z \lesssim 1.7$ (similar to that of our sample here). No difference is seen between the Hα and stellar continuum sizes in less massive galaxies ($8.96 < \log(M_*/M_\odot) < 9.25$), but the H$\alpha$ sizes are slightly larger than the stellar continuum for more massive galaxies ($9.70 < \log(M_*/M_\odot) < 11.3$). We similarly observe that the median NUV-band effective radius is $1.15^{+0.09}_{-0.04}$ times larger than that of the stellar continuum in galaxies with $9 < \log(M_*/M_\odot) < 9.45$ and at $z \leqslant 1.2$. Therefore the NUV and Hα morphologies provide reinforcing evidence for this "inside-out" growth, at least for galaxies at lower stellar masses.

On the other hand, we find that the PAH emission on average is slightly *smaller* (~10%) than the stellar continuum in galaxies with $M_* \gtrsim 10^{9.5} M_\odot$ at $z \leqslant 1.2$, and the sizes of PAH emission and stellar continuum are similar in galaxies with lower stellar masses (see Figure 8). For galaxies at higher stellar masses, the fact that the sizes of the PAH emission are smaller than the stellar continuum implies that there is an increase in dust-obscured star formation in the central regions of galaxies, and that this increases with the stellar mass. This result is consistent with the stellar mass dependence on the extent of dust attenuation using Balmer decrements of Hα/Hβ (Nelson et al. 2016b) and UV continuum Tacchella (et al. 2018).

Previous studies have explored the evolution of the sizes of the rest-frame far-IR continuum measurements from ALMA as a tracer of the obscured star formation. These studies generally revealed that the dust-obscured star formation is much more compact compared to the stellar continuum (Hodge et al. 2015; Simpson et al. 2015; Chen et al. 2017; Fujimoto et al. 2017; Tadaki et al. 2017a, 2017b, 2020; Calistro Rivera et al. 2018; Gullberg et al. 2019; Hodge et al. 2019; Lang et al. 2019; Cheng et al. 2020; Gómez-Guijarro et al. 2022). However, these ALMA results have been limited almost entirely to galaxies more massive than $M_* \gtrsim 10^{10.5} M_\odot$, which is even higher than our highest mass bin. In our highest mass bin ($\log(M_*/M_\odot) = 10 - 10.5$ at $z > 1.2$), we find that the sizes of galaxies in the PAH band are similar to those in the F160W. This is potentially inconsistent with the ALMA results, even we consider a 10% decrease in the size ratio of the PAH band to F160W between galaxies with $\log(M_*/M_\odot) = 10 - 10.5$

and galaxies with $\log(M_*/M_\odot) > 10.5$ are assumed based on the decrease observed in the low-redshift subsample, while our highest mass bin contains only 15 galaxies, with a large spread in the $R_{\rm eff}$ ratio of the PAH band to F160W (see Figure 8). Based on the trend between the galaxy sizes in the PAH band and F160W from the low-redshift subsample, we expect this is evidence that the dust-obscured star formation becomes more compact with increasing mass, which could connect the MIRI-based sizes here with the ALMA ones in the literature. Although, it might be possible that the physical scales measured from ALMA are affect by the interferometry that missed the diffuse far-IR emission and underestimate the extent of far-IR emission. These issues will be discussed further by B. Magnelli et al. (2023, in preparation).

Therefore, the interpretation of the NUV and PAH sizes is enigmatic. One possibility is that the NUV and PAH emission trace star formation on different timescales (where the NUV traces the direct continuum from OB-type stars with lifetimes of ∼10–100 Myr while the PAH and IR emission can include heating from longer-lived stellar stars with lifetimes of 500 Myr to 1 Gyr; Salim et al. 2009; Kennicutt & Evans 2012; Salim & Narayanan 2020). It is therefore plausible that if galaxies grow and quench via an "inside-out" process, the PAH appearances would lag behind that of the UV. This can account for the growth of galaxies, at least at lower stellar masses.

However, at higher stellar masses, our PAH results do not favor this "inside-out" scenario as that PAH-based effective radii become smaller than that of the NUV or of the stellar continuum. This favors an interpretation that star formation is increasingly obscured and more centrally concentrated. This is apparent by the fact that $\rm SFR_{IR}$ and $\Sigma_{\rm IR}$ is higher than $\rm SFR_{UV}$ and $\Sigma_{\rm UV}$ for galaxies with $\log(M_*/M_\odot) \gtrsim 9.5$, and that the fraction of the IR SFR increases to higher stellar masses (Figure 10). The observation that the star formation in SFGs becomes more compact as the galaxies grow in mass has important ramifications for their evolution. For example, it will be important to test if the SFR surface densities versus the galaxy stellar mass connect to predictions for bulge growth in galaxies (including if galaxies "compactify;" e.g., Ceverino et al. 2010; Dekel & Burkert 2014; Zolotov et al. 2015; Tacchella et al. 2016) and if galaxy quenching occurs when the stellar mass or the stellar mass surface density reach some critical value. This can be tested by future studies with larger samples, particularly for larger samples of more massive galaxies with MIRI coverage.

Another possible explanation might be that the contribution by older stellar populations (as opposed to the forming ones) to the excitation of the PAH grains is proportionally larger in more massive galaxies. Thus, in their central regions, a larger fraction of the PAH emission is being excited by existing stars in massive galaxies than that in lower-mass galaxies, which is shown as higher $\Sigma_{\rm IR}$. Other reasons also include that the complex morphology of massive high-redshift galaxies makes it difficult to reproduce the mass/light distribution with a single-component model, such as compact bulges being formed (Costantin et al. 2021, 2022a; Guo et al. 2023).

Nevertheless, from various simulations, the effect of dust obscuration has been pointed out as one of the reasons for the discrepancy in the intrinsic and observed size of massive galaxies observed in rest-frame optical wavelength (Costantin et al. 2022b) and also at rest-frame far-UV (Marshall et al. 2022; Roper et al. 2022). This is supported by previous studies, which found the half-mass radii is, on average, smaller than the half-light radii for galaxies with stellar mass $\gtrsim 10^{10} M_\odot$ at $1.0 \leqslant z \leqslant 2.5$ (Suess et al. 2019). The PAH-band size–mass relation from this paper seems to follow the intrinsic size–mass relation from these simulations that decreases with increasing stellar mass. Thus, the PAH or MIR morphology could help in correcting the rest-frame optical/FIR and rest-frame UV or Hα morphology and to obtain an intrinsic size–mass relation, which can in turn inform the formation and quenching mechanisms.

6. Summary

We use imaging from JWST/MIRI covering 7.7–21 μm to study the morphologies of galaxies based on their PAH emission. The MIRI data resolve angular structures in galaxies on scales of 0.″1–0.″3 and allow for the first time a quantitative measurement of galaxy morphologies in the mid-IR for the first time.

We compare the morphologies of 64 star-forming galaxies at $0.2 < z < 2.5$ with stellar mass $\log(M_*) > 10^9\ M_\odot$ in their in PAH band, NUV band, and F160W using data form JWST MIRI, HST ACS/F435W or ACS/F606W, and HST WFC3/160W. These three bands trace the profiles of obscured, unobscured star formation, and stellar continuum, respectively. We found there are differences in the galaxy morphologies in their PAH band, NUV band, and F160W, which depend on the stellar mass and redshift. Our results are summarized as follows:

1. Comparing to the sizes of galaxies in the stellar continuum traced by F160W to the obscured star formation traced by the PAH band, we find that the latter are slightly smaller size (in $R_{\rm eff}$) with a similar fraction of light within 1 kpc (similar in $f_{\rm 1\ kpc}$) for galaxies with $\log(M_*) \gtrsim 10^{9.5} M_\odot$ at $z \leqslant 1.2$.
2. Comparing the sizes of galaxies in the stellar continuum traced by F160W to the unobscured star formation traced by the NUV band, we find that the latter is larger (in $R_{\rm eff}$) and more extended (lower in $f_{\rm 1\ kpc}$) for galaxies at $z \leqslant 1.2$, but the NUV-band and F160W values are more similar for galaxies at $z \leqslant 1.2$.
3. The average Sérsic indices of galaxies measured in their NUV and PAH bands are similar with ($\langle n \rangle \sim 0.7$). These are both smaller than the average Sérsic indices measured in the F160W band ($\langle n \rangle = 1.1$). These results reveal that the stellar continuum prefers a disk-like profile, while the obscured and unobscured star formation follow a flatter profile (within the effective radius).
4. We estimate the surface density of the SFR and stellar mass density, by combining information from the morphological tracers of star formation (the NUV and PAH bands) with the total SFR (from UV and far-IR data), and using morphological tracers of the stellar continuum (from the F160W data) with the total stellar mass. We find that the surface density of the SFR derived from IR increases faster with increasing stellar mass (i.e., it has a steeper slope) than the surface density of the SFR derived from UV. We interpret this as evidence that galaxies with higher stellar masses have preferentially higher amounts of centrally concentrated dust-obscured star formation.

5. The surface density of the SFR derived from the IR also increases with the stellar mass with a steeper slope than the surface density of stellar mass at $z \leqslant 1.2$, suggesting that massive SFGs, at least at $z \leqslant 1.2$, experience a faster buildup of their dust content in their inner regions compared to their stellar mass. At $z > 1.2$, the relation between the IR-based SFR surface density and mass has a similar slope as the stellar mass surface density and mass, possible due to the lack of low-mass galaxies with $M_* \lesssim 10^{9.5} M_\odot$.
6. We study the fraction of obscured star formation (defined as the ratio of the IR-based SFR to the total IR + UV SFR), both measured within 1 kpc and integrated over the entire galaxy. We find a strong correlation between the fraction of obscured star formation and stellar mass, both for the fraction measured within 1 kpc, and the fraction integrated over the entire galaxy. The obscured fraction is generally lower for lower-mass galaxies ($f_{\rm obs} \sim 0.5$ for masses of $10^{9-9.5}\,M_\odot$) than for more massive galaxies ($f_{\rm obs} \gtrsim 0.7$ for masses of $\gtrsim 10^{9.5}\,M_\odot$), suggesting that dust attenuation is not a primary cause for the more extended NUV in these low-mass galaxies.

This paper demonstrates the capability of MIRI data to reveal the morphology of dust-obscured star-forming regions in star-forming galaxies down to $M_* \sim 10^9\,M_\odot$. We expect that future MIRI surveys will provide a more complete sample to study the morphology of obscured star formation and dust attenuation, which can inform the spatially resolved growth of galaxies and the intrinsic size–mass relation.

We acknowledge the hard work of our colleagues in the CEERS and UVCANDELS collaboration and everyone involved in the JWST mission. This work benefited from support from the George P. and Cynthia Woods Mitchell Institute for Fundamental Physics and Astronomy at Texas A&M University. C.P. thanks Marsha and Ralph Schilling for generous support of this research. R.A.W. acknowledges support from NASA JWST Interdisciplinary Scientist grants NAG5-12460, NNX14AN10G and 80NSSC18K0200 from GSFC. This work acknowledges support from the NASA/ESA/CSA James Webb Space Telescope through the Space Telescope Science Institute, which is operated by the Association of Universities for Research in Astronomy, Incorporated, under NASA contract NAS5-03127. Support for program No. JWST-ERS01345 was provided through a grant from the STScI under NASA contract NAS5-03127. This work is based on observations with the NASA/ESAHubble Space Telescope obtained at the Space Telescope Science Institute, which is operated by the Association of Universities for Research in Astronomy, Incorporated, under NASA contract NAS5-26555. Support for Program number HST-GO-15647 was provided through a grant from the STScI under NASA contract NAS5-26555.

ORCID iDs

Lu Shen https://orcid.org/0000-0001-9495-7759
Casey Papovich https://orcid.org/0000-0001-7503-8482
Guang Yang https://orcid.org/0000-0001-8835-7722
Jasleen Matharu https://orcid.org/0000-0002-7547-3385
Xin Wang https://orcid.org/0000-0002-9373-3865
Benjamin Magnelli https://orcid.org/0000-0002-6777-6490
David Elbaz https://orcid.org/0000-0002-7631-647X
Shardha Jogee https://orcid.org/0000-0002-1590-0568
Anahita Alavi https://orcid.org/0000-0002-8630-6435
Pablo Arrabal Haro https://orcid.org/0000-0002-7959-8783
Bren E. Backhaus https://orcid.org/0000-0001-8534-7502
Micaela B. Bagley https://orcid.org/0000-0002-9921-9218
Eric F. Bell https://orcid.org/0000-0002-5564-9873
Laura Bisigello https://orcid.org/0000-0003-0492-4924
Antonello Calabrò https://orcid.org/0000-0003-2536-1614
M. C. Cooper https://orcid.org/0000-0003-1371-6019
Luca Costantin https://orcid.org/0000-0001-6820-0015
Emanuele Daddi https://orcid.org/0000-0002-3331-9590
Mark Dickinson https://orcid.org/0000-0001-5414-5131
Steven L. Finkelstein https://orcid.org/0000-0001-8519-1130
Seiji Fujimoto https://orcid.org/0000-0001-7201-5066
Mauro Giavalisco https://orcid.org/0000-0002-7831-8751
Norman A. Grogin https://orcid.org/0000-0001-9440-8872
Yuchen Guo https://orcid.org/0000-0002-4162-6523
Benne W. Holwerda https://orcid.org/0000-0002-4884-6756
Jeyhan S. Kartaltepe https://orcid.org/0000-0001-9187-3605
Anton M. Koekemoer https://orcid.org/0000-0002-6610-2048
Peter Kurczynski https://orcid.org/0000-0002-8816-5146
Ray A. Lucas https://orcid.org/0000-0003-1581-7825
Pablo G. Pérez-González https://orcid.org/0000-0003-4528-5639
Nor Pirzkal https://orcid.org/0000-0003-3382-5941
Laura Prichard https://orcid.org/0000-0002-0604-654X
Marc Rafelski https://orcid.org/0000-0002-9946-4731
Kaila Ronayne https://orcid.org/0000-0001-5749-5452
Raymond C. Simons https://orcid.org/0000-0002-6386-7299
Ben Sunnquist https://orcid.org/0000-0003-3759-8707
Harry I. Teplitz https://orcid.org/0000-0002-7064-5424
Jonathan R. Trump https://orcid.org/0000-0002-1410-0470
Benjamin J. Weiner https://orcid.org/0000-0001-6065-7483
Rogier A. Windhorst https://orcid.org/0000-0001-8156-6281
L. Y. Aaron Yung https://orcid.org/0000-0003-3466-035X

References

Acquaviva, V., Gawiser, E., & Guaita, L. 2012, in IAU Symp. 284, The Spectral Energy Distribution of Galaxies—SED 2011, ed. R. J. Tuffs & C. C. Popescu (Cambridge: Cambridge Univ. Press), 42
Bagley, M. B., Finkelstein, S. L., Koekemoer, A. M., et al. 2022, ApJL, 946, L12
Barro, G., Faber, S. M., Koo, D. C., et al. 2017, ApJ, 840, 47
Barro, G., Pérez-González, P. G., Gallego, J., et al. 2011, ApJS, 193, 13
Bell, E. F., Papovich, C., Wolf, C., et al. 2005, ApJ, 625, 23
Bolzonella, M., Miralles, J. M., & Pelló, R. 2000, A&A, 363, 476
Boquien, M., Burgarella, D., Roehlly, Y., et al. 2019, A&A, 622, A103
Bruzual, G., & Charlot, S. 2003, MNRAS, 344, 1000
Calistro Rivera, G., Hodge, J. A., Smail, I., et al. 2018, ApJ, 863, 56
Calzetti, D. 2001, PASP, 113, 1449
Calzetti, D., Armus, L., Bohlin, R. C., et al. 2000, ApJ, 533, 682
Calzetti, D., Kennicutt, R. C., Engelbracht, C. W., et al. 2007, ApJ, 666, 870
Ceverino, D., Dekel, A., & Bournaud, F. 2010, MNRAS, 404, 2151
Chabrier, G. 2003, PASP, 115, 763
Chen, C.-C., Hodge, J. A., Smail, I., et al. 2017, ApJ, 846, 108
Cheng, C., Ibar, E., Smail, I., et al. 2020, MNRAS, 499, 5241
Cheung, E., Faber, S. M., Koo, D. C., et al. 2012, ApJ, 760, 131
Ciotti, L., & Bertin, G. 1999, A&A, 352, 447
Cooper, M. C., Griffith, R. L., Newman, J. A., et al. 2012, MNRAS, 419, 3018

Costantin, L., Pérez-González, P. G., Méndez-Abreu, J., et al. 2021, ApJ, 913, 125
Costantin, L., Pérez-González, P. G., Méndez-Abreu, J., et al. 2022a, ApJ, 929, 121
Costantin, L., Pérez-González, P. G., Vega-Ferrero, J., et al. 2022b, arXiv:2208.00007
Dale, D. A., & Helou, G. 2002, ApJ, 576, 159
Davis, M., Guhathakurta, P., Konidaris, N. P., et al. 2007, ApJL, 660, L1
Dekel, A., & Burkert, A. 2014, MNRAS, 438, 1870
Dekel, A., Sari, R., & Ceverino, D. 2009, ApJ, 703, 785
Draine, B. T., Aniano, G., Krause, O., et al. 2014, ApJ, 780, 172
Estrada-Carpenter, V., Papovich, C., Momcheva, I., et al. 2020, ApJ, 898, 171
Fontana, A., D'Odorico, S., Poli, F., et al. 2000, AJ, 120, 2206
Fossati, M., Gavazzi, G., Savorgnan, G., et al. 2013, A&A, 553, A91
Fujimoto, S., Ouchi, M., Shibuya, T., & Nagai, H. 2017, ApJ, 850, 83
Fukugita, M., Ichikawa, T., Gunn, J. E., et al. 1996, AJ, 111, 1748
Gardner, J. P., Mather, J. C., Clampin, M., et al. 2006, SSRv, 123, 485
Gómez-Guijarro, C., Elbaz, D., Xiao, M., et al. 2022, A&A, 659, A196
Graham, A. W., & Driver, S. P. 2005, PASA, 22, 118
Graham, A. W., Driver, S. P., Petrosian, V., et al. 2005, AJ, 130, 1535
Grogin, N. A., Kocevski, D. D., Faber, S. M., et al. 2011, ApJS, 197, 35
Gullberg, B., Smail, I., Swinbank, A. M., et al. 2019, MNRAS, 490, 4956
Guo, Y., Jogee, S., Finkelstein, S. L., et al. 2023, ApJL, 945, L10
Häussler, B., McIntosh, D. H., Barden, M., et al. 2007, ApJS, 172, 615
Hodge, J. A., Riechers, D., Decarli, R., et al. 2015, ApJL, 798, L18
Hodge, J. A., Smail, I., Walter, F., et al. 2019, ApJ, 876, 130
Ilbert, O., Arnouts, S., McCracken, H. J., et al. 2006, A&A, 457, 841
James, P. A., Bretherton, C. F., & Knapen, J. H. 2009, A&A, 501, 207
Ji, Z., & Giavalisco, M. 2022, ApJ, 935, 120
Jin, S., Daddi, E., Liu, D., et al. 2018, ApJ, 864, 56
Kelly, B. C. 2007, ApJ, 665, 1489
Kennicutt, R. C., & Evans, N. J. 2012, ARA&A, 50, 531
Kennicutt, R. C., Jr. 1998, ARA&A, 36, 189
Koekemoer, A. M., Faber, S. M., Ferguson, H. C., et al. 2011, ApJS, 197, 36
Kriek, M., Shapley, A. E., Reddy, N. A., et al. 2015, ApJS, 218, 15
Kriek, M., van Dokkum, P. G., Labbé, I., et al. 2009, ApJ, 700, 221
Laird, E. S., Nandra, K., Georgakakis, A., et al. 2009, ApJS, 180, 102
Lang, P., Schinnerer, E., Smail, I., et al. 2019, ApJ, 879, 54
Lee, S.-K., Ferguson, H. C., Somerville, R. S., Wiklind, T., & Giavalisco, M. 2010, ApJ, 725, 1644
Liu, D., Daddi, E., Dickinson, M., et al. 2018, ApJ, 853, 172
MacArthur, L. A., Courteau, S., & Holtzman, J. A. 2003, ApJ, 582, 689
Madau, P., & Dickinson, M. 2014, ARA&A, 52, 415
Marshall, M. A., Wilkins, S., Di Matteo, T., et al. 2022, MNRAS, 511, 5475
Masters, D. C., Stern, D. K., Cohen, J. G., et al. 2017, ApJ, 841, 111
Matharu, J., Muzzin, A., Brammer, G. B., et al. 2019, MNRAS, 484, 595
Matharu, J., Papovich, C., Simons, R. C., et al. 2022, ApJ, 937, 16
Mehta, V., Teplitz, H. I., Scarlata, C., et al. 2022, arXiv:2211.02056
Merlin, E., Bourne, N., Castellano, M., et al. 2016, A&A, 595, A97
Momcheva, I. G., Brammer, G. B., van Dokkum, P. G., et al. 2016, ApJS, 225, 27
Murphy, E. J., Chary, R. R., Dickinson, M., et al. 2011, ApJ, 732, 126
Nandra, K., Laird, E. S., Adelberger, K., et al. 2005, MNRAS, 356, 568
Nandra, K., Laird, E. S., Aird, J. A., et al. 2015, ApJS, 220, 10
Nelson, E. J., van Dokkum, P. G., Brammer, G., et al. 2012, ApJL, 747, L28
Nelson, E. J., van Dokkum, P. G., Förster Schreiber, N. M., et al. 2016a, ApJ, 828, 27
Nelson, E. J., van Dokkum, P. G., Momcheva, I. G., et al. 2016b, ApJL, 817, L9
Newman, J. A., Cooper, M. C., Davis, M., et al. 2013, ApJS, 208, 5
Oke, J. B., & Gunn, J. E. 1983, ApJ, 266, 713
Papovich, C., Cole, J., Yang, G., et al. 2022, arXiv:2301.00027
Peng, C. Y., Ho, L. C., Impey, C. D., & Rix, H.-W. 2002, AJ, 124, 266
Peng, C. Y., Ho, L. C., Impey, C. D., & Rix, H.-W. 2010, AJ, 139, 2097
Rafelski, M., Teplitz, H. I., Gardner, J. P., et al. 2015, AJ, 150, 31
Roper, W. J., Lovell, C. C., Vijayan, A. P., et al. 2022, MNRAS, 514, 1921
Salim, S., Dickinson, M., Michael Rich, R., et al. 2009, ApJ, 700, 161
Salim, S., & Narayanan, D. 2020, ARA&A, 58, 529
Sérsic, J. L. 1963, BAAA, 6, 41
Shen, L., Lemaux, B. C., Lubin, L. M., et al. 2020, MNRAS, 494, 5374
Shen, S., Mo, H. J., White, S. D. M., et al. 2003, MNRAS, 343, 978
Shipley, H. V., Papovich, C., Rieke, G. H., Brown, M. J. I., & Moustakas, J. 2016, ApJ, 818, 60
Shipley, H. V., Papovich, C., Rieke, G. H., et al. 2013, ApJ, 769, 75
Simpson, J. M., Smail, I., Swinbank, A. M., et al. 2015, ApJ, 799, 81
Skelton, R. E., Whitaker, K. E., Momcheva, I. G., et al. 2014, ApJS, 214, 24
Smith, J. D. T., Draine, B. T., Dale, D. A., et al. 2007, ApJ, 656, 770
Stefanon, M., Yan, H., Mobasher, B., et al. 2017, ApJS, 229, 32
Suess, K. A., Kriek, M., Price, S. H., & Barro, G. 2019, ApJ, 877, 103
Suess, K. A., Kriek, M., Price, S. H., & Barro, G. 2021, ApJ, 915, 87
Tacchella, S., Carollo, C. M., Förster Schreiber, N. M., et al. 2018, ApJ, 859, 56
Tacchella, S., Carollo, C. M., Renzini, A., et al. 2015, Sci, 348, 314
Tacchella, S., Dekel, A., Carollo, C. M., et al. 2016, MNRAS, 458, 242
Tadaki, K.-i., Belli, S., Burkert, A., et al. 2020, ApJ, 901, 74
Tadaki, K.-i., Genzel, R., Kodama, T., et al. 2017a, ApJ, 834, 135
Tadaki, K.-i., Kodama, T., Nelson, E. J., et al. 2017b, ApJL, 841, L25
Teplitz, H. I., Rafelski, M., Kurczynski, P., et al. 2013, AJ, 146, 159
van der Wel, A., Franx, M., van Dokkum, P. G., et al. 2014, ApJ, 788, 28
van Dokkum, P. G., Nelson, E. J., Franx, M., et al. 2015, ApJ, 813, 23
Weinzirl, T., Jogee, S., Conselice, C. J., et al. 2011, ApJ, 743, 87
Whitaker, K. E., Kriek, M., van Dokkum, P. G., et al. 2012, ApJ, 745, 179
Whitaker, K. E., Pope, A., Cybulski, R., et al. 2017, ApJ, 850, 208
Wiklind, T., Dickinson, M., Ferguson, H. C., et al. 2008, ApJ, 676, 781
Williams, R. J., Quadri, R. F., Franx, M., van Dokkum, P., & Labbé, I. 2009, ApJ, 691, 1879
Wilman, D. J., Fossati, M., Mendel, J. T., et al. 2020, ApJ, 892, 1
Wu, Y., Helou, G., Armus, L., et al. 2010, ApJ, 723, 895
Wuyts, S., Förster Schreiber, N. M., van der Wel, A., et al. 2011, ApJ, 742, 96
Xie, Y., & Ho, L. C. 2019, ApJ, 884, 136
Yang, G., Boquien, M., Buat, V., et al. 2020, MNRAS, 491, 740
Zhou, R., Cooper, M. C., Newman, J. A., et al. 2019, MNRAS, 488, 4565
Zolotov, A., Dekel, A., Mandelker, N., et al. 2015, MNRAS, 450, 2327